Strong-field photoemission dynamics from metallic nanostructures

Sambit Mitra

30th June, 2016

Master Thesis

External supervisor: Prof. Dr. Matthias Kling

Internal supervisor: Prof. Dr. Manfred Kappes

In partial fulfillment of the degree: Master of Science in Optics and Photonics of the Karlsruhe School of Optics and Photonics, Karlsruhe Institute of Techonology, Karlsruhe. Performed externally at the Max Planck Institute of Quantum Optics, Garching b. München.

Declaration

Ich versichere wahrheitsgemäß, die Arbeit selbstständig verfasst, alle benutzten Hilfsmittel vollständig und genau angegeben und alles kenntlich gemacht zu haben, was aus Arbeiten anderer unverändert oder mit Abänderungen entnommen wurde sowie die Satzung des KIT zur Sicherung guter wissenschaftlicher Praxis in der jeweils gültigen Fassung beachtet zu haben.

(English)

I herewith declare that the present thesis is original work written by me alone, that I have indicated completely and precisely all aids used as well as all citations, whether changed or unchanged, of other theses and publications, and that I have observed the KIT Statutes for Upholding Good Scientific Practice, as amended.

Garching b. München, 30^{th} June 2016

Sambit Mitra

Abstract

This thesis observes and analyses electron emission from the apex of gold nanotips under the influence of few-cycle laser pulses. The aim of the work was to study the emission process in the strong-field regime, where electron emission is predominantly driven by tunneling. Laser induced tunneling is a highly non-linear process which is driven by the electric field of the carrier wave in a laser pulse. This makes it extremely sensitive to changes in the carrier-envelope-phase (CEP). Thereby, field-driven processes such as tunneling enable time-resolved measurements down to attosecond timescales.

The emission dynamics are studied in terms of the terminal kinetic energy and yield of the electrons photoemitted from the metal surface. Emission occurs when the few-cycle pulses are tightly focussed on the tip apex, after which the energy spectrum is recorded by a time-of-flight electron spectrometer. The measurements are carried out at an intensity range of $10^{11} - 10^{12}\,\mathrm{W/cm^2}$. Due to field-enhancement in nanostructures (plasmonic and non-plasmonic), the effective intensities are amplified almost by an order of magnitude, reaching pulse electric field strengths needed for strong-field emission. The experiment is performed and analyzed under two conditions. One, with few-cycle pulses at a wavelength of 700 nm and the second at 1800 nm.

CEP resolved measurements are performed with 700 nm laser pulses with varying laser intensities. The emission dynamics are analyzed primarily based on their electron count scaling with intensity and their modulation with the CEP. The observed count scaling indicates electron emission in the weak-field regime (multiphoton emission). The energy spectra exhibit strong CEP dependence for the high-energy electrons, indicating coexistence of strong-field emission (tunneling). However, the electron yield for strong-field emission was found to be three to four orders of magnitude below the weak-field emission.

Intensity varying measurements are also carried out with the 1800 nm laser pulses. Similar data analysis techniques were performed, which indicate the majority of the electrons being emitted by the strong-field mechanism. A sharp narrow bandwidth ($\approx$0.2 eV) peak is observed in the low-energy region of the measured spectra, whose position shifts with intensity. This behavior of the low-energy peak has not been observed or discussed previously. They are analyzed and reproduced by simulations in the strong-field framework. The investigation explains the behavior in terms of the terminal kinetic energy of tunneled and re-scattered electrons, modified by the laser induced near-field gradients.

Contents

Chapter 1

Introduction

1.1 Motivation

The term static, is used to label any phenomenon that does not change with time. However, what appears static to our eye, may not be so in reality. The fast moving blades of a mechanical fan appears like a static blur, but a sufficiently bright, quick flash of light incident on the fan can reveal the instantaneous position of the blades. Taking multiple snap shots at different times, forms a reconstruction of its behavior. The same idea is used to observe fast molecular and atomic motion which require laser pulses that only last a few femtoseconds ($1\,\text{fs} = 10^{-15}\,\text{s}$) [2]. Even shorter laser pulses allow resolving dynamics of electrons in atoms and molecules occurring at attosecond ($1\,\text{as} = 10^{-18}$ s) timescales [3, 1]. The length and time scales at which different structures reveal their dynamics are represented in a graphical form in Figure 1.1.

Lately, there has been growing interest in carrying out similar studies with electron pulses [4]. An advantage of electron beams over lasers is its direct imaging ability of structural dynamics as compared to lasers which are used to obtain frequency and time resolved data. Two related examples are dynamic transmission electron microscopy (DTEM) where time-resolved real-space images are obtained, and ultra-fast electron diffraction (UED) which provides time-resolved structural information by diffraction. A detailed review of these and other applications of electron pulses can be found in [4].

With the possibility of interesting applications, it is important to obtain a suitable source for pulsed electron emission. For a long time, electron pulses have been produced by focussing high-power femtosecond laser pulses on a photocathode [5]. In this case, the emission area is determined by the laser focal spot size, which is on the order of microns. Later, electron pulses as short as 70 fs with an emission diameter of 2 nm was demonstrated [6]. This was obtained by focussing femtosecond laser pulses at the apex of a metal nanotip. Such small emission regions improve the spatial imaging resolution of the electron beams. Electron emission from metallic nanotips are also obtained by field-emission, i.e when a large negative bias voltage is applied with respect to its surroundings. Field-emission generates electrons of a very narrow energy width

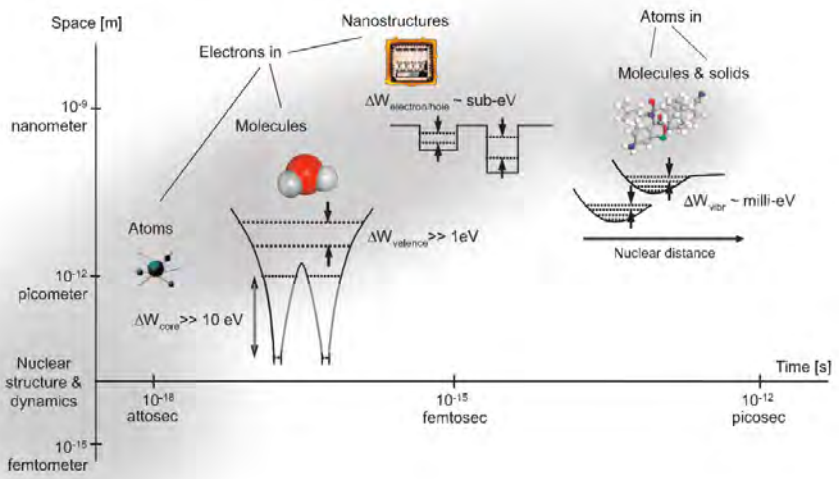

Figure 1.1: **Time and length scales necessary for resolving dynamics of respective structures in the microcosm.** [1]

(≈0.2 eV) reducing aberrations caused by electron optics [7]. Thus, tip-based pulsed electron sources are a promising candidate for an ultra-short pulsed electron source applications.

In this thesis, electron emission dynamics have been studied and analyzed at the apex of gold nanotips with the aim of extending its current understanding at sub-femtosecond timescales. This would help in the development of an ideal, ultra-fast pulsed electron source, which requires precise control over the spatial profile, energy-bandwidth and temporal profile of the emission. An artistic representation of the process is shown in Figure 1.2.

1.2 Outline

The thesis is organized in six chapters. After Chapter 1, Chapter 2 gives a background on key concepts which are used to realize the laser induced electron emission and its analysis. This involves a description of ultra-short laser pulses which operate in a few-cycle and phase stable configuration. After which, a description of how the laser electric fields are amplified at a nanotip apex are presented, followed by a description of electron emission mechanisms from metal surfaces. Chapter 3 presents the experimental details of the laser sources, setup for generating and detecting electron emission along with some of the data acquisition techniques. Chapter 4 describes a theoretical model for simulations, which are carried out to understand the experimental data. Chapter 5 reports and analyses the experimental findings of the work along

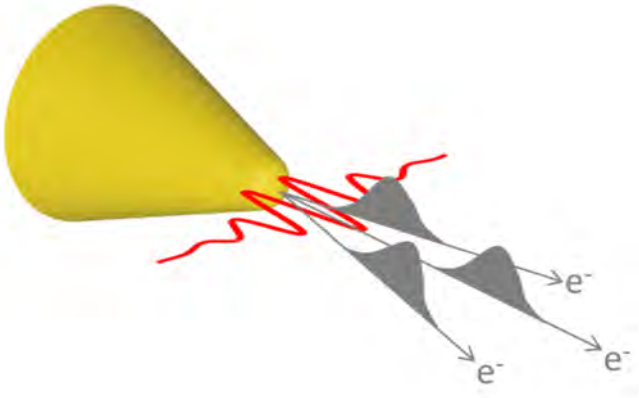

Figure 1.2: **Artistic representation of strong-field phenomenon at a gold nanotip.** The central idea of this thesis is captured in the figure. A gold nanotip (in yellow) is irradiated with ultra-short high intensity laser pulses. Short enough that the evolution of the electric field cycles (in red) are clearly distinguishable. This leads to electron emission (in gray) arising from various processes, some of which have been reported and analyzed in this thesis.

with a comparison with simulations in some cases. Finally, Chapter 6 summarizes the findings of this work along with an outlook which suggests future ideas to support the findings of this work.

Chapter 2

Background

This chapter provides an overview of theoretical concepts needed to investigate electron emission at ultra-fast timescales. Starting with a description of the laser pulses used, it goes on to describe how the electric field of the laser pulses are amplified in the vicinity of a metallic nanotip. After which, the chapter describes light-matter interactions governing electron emission from metallic surfaces.

2.1 Ultra-short laser pulses

The study of electron emission at sub-femtosecond timescales, requires suitable laser pulses. It becomes important to gain control over the instantaneous electric field variation of the carrier wave[1] within a laser pulse. This is only possible with the use of a *few-cycle* laser pulse. In this section, few-cycle pulses are defined, followed by description of how they are used to modify the electric field amplitude of the carrier wave.

2.1.1 Few-cycle pulse

The electric field evolution of a laser pulse can be expressed as the product of a Gaussian function and an oscillatory cosine function, written as

$$E(t) = E_0 e^{-2\ln 2 \frac{t^2}{\Delta\tau^2}} \cos(\omega_0 t - \varphi)\,, \tag{2.1}$$

where $\Delta\tau$ is the pulse duration (full width at half maximum of the average intensity), ω_0 is the frequency of field oscillation and φ is the phase of the cosine function, which represents the carrier wave. In reality, pulsed lasers propagate with a broad range of wave frequencies. These waves add up to an amplitude modulated pulse where their weighted mean frequency is ω_0 (center frequency). All this, assuming that the

[1] A wave oscillating at a frequency which is the weighted mean of all the wave frequencies present in the laser radiation

pulse is chirp free, i.e there is no time dependent frequency shift in the carrier wave. In this case, the pulses are also limited by an uncertainty relationship known as the time-bandwidth product, or Fourier limit. It is defined as

$$\Delta\tau\Delta\upsilon \geq 0.44\,, \tag{2.2}$$

in case of Gaussian shaped pulses, where $\Delta\upsilon$ is the frequency bandwidth. As a consequence, ultra-short pulses require lasers which can produce large frequency bandwidth radiation.

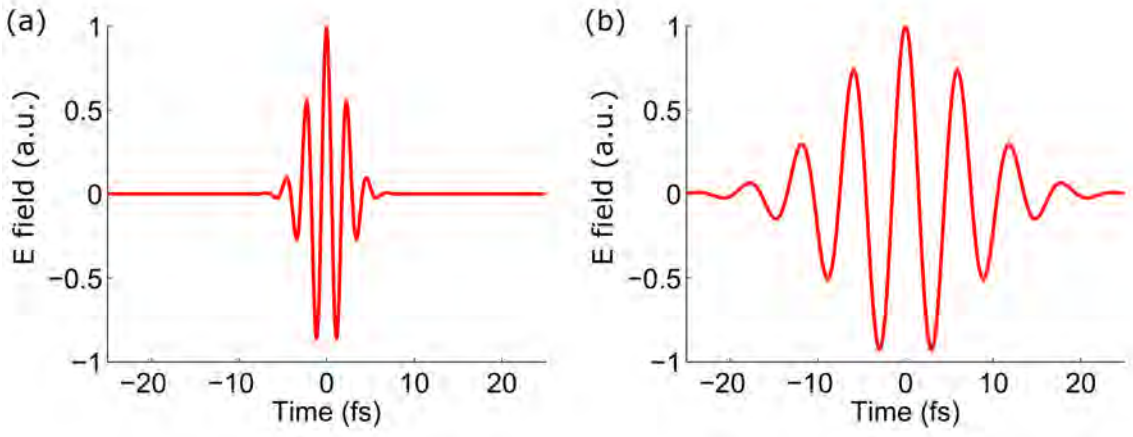

Figure 2.1: **Calculated electric field evolution of the laser pulses used in our experiment.** (a) Pulse duration: 5 fs, central wavelength: 700 nm. (b) Pulse duration: 18 fs, central wavelength: 1800 nm.

To detect changes in electron emission, purely based on changes in the electric field amplitude, it is important to be able to modulate the amplitudes without changing the average intensity. In-case of a continuous wave laser (without forming pulses), it would be impossible to change this amplitude without changing the average intensity. However, depending on the center frequency of the laser, if the pulse duration is short enough, it can produce large contrast between the peak electric field amplitudes of successive cycles. This configuration is known as a few-cycle pulse (see Figure 2.1). The electric field amplitude can now be modulated by changing the phase of the cosine function (see Equation 2.1) or the carrier wave. Thus it becomes essential to precisely control this phase, more commonly termed as the carrier envelope phase (CEP).

2.1.2 CEP and its detection

As described before, the amplitude of different electric field cycles in few-cycle pulses depends on the CEP (see Figure 2.2 (a)). The absolute value of CEP is already present in equation 2.1, as φ. The first step in controlling this parameter is its detection. It not only allows us to tag the CEP during measurements, but also as a feedback

for stabilizing fluctuations in it arising from the laser cavity and turbulence[2] in the propagating medium.

Figure 2.2 shows the time domain representations of the output from a mode-locked laser cavity. The modulations in the envelope of the pulses are brought about by the interference of frequencies which are allowed to resonate in the laser cavity. In the frequency domain, they correspond to a frequency comb with a comb spacing equal to f_{rep}, the repetition rate of the laser.

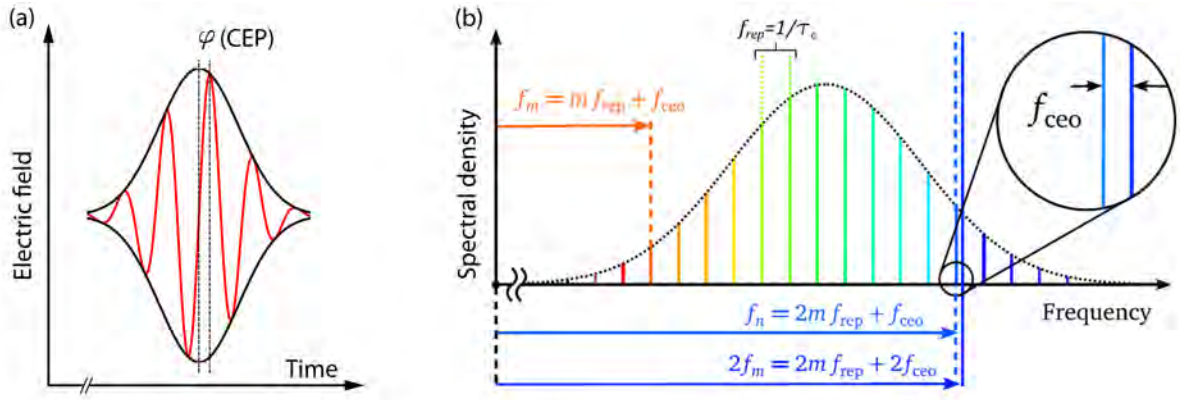

Figure 2.2: **Time and frequency domain representation of a few-cycle pulse.** (a) The CEP is expressed as φ,the phase difference between the envelope and the carrier. (b) Frequency comb of the corresponding laser pulse. f_{rep} is the repetition rate of the laser, τ_c is the cavity round trip time, f_{ceo} is the carrier-envelope-offset frequency, f_m and f_n are two specific frequencies in the comb [8].

The CEP is modified by the difference between velocity of the carrier wave with respect to the pulse envelope which are defined by the phase velocity $v_{ph} = \omega/k$ and group velocity $v_g = d\omega/dk$, respectively. The parameter $\Delta\varphi$, is defined as the pulse to pulse phase slip introduced in the laser cavity, and other dispersive media[3]. The phase slip is expressed in the frequency domain in terms of a parameter f_{ceo}, the carrier-envelope offset frequency [9]

$$\Delta\varphi = 2\pi \frac{f_{ceo}}{f_{rep}} . \tag{2.3}$$

where f_{rep} is the repetition rate of laser pulses and a known quantity. From this, the pulse to pulse CEP shift $\Delta\varphi$ in the time domain, can be determined from the offset frequency f_{ceo}, in the frequency domain. The offset-frequency is commonly detected using a technique called self-referencing [10]. In this technique, the pulses are spatially

[2]Time varying density of air leading to time varying refractive index
[3]A medium with a wavelength dependent refractive index $n(\lambda)$

separated in two parts. One undergoes second harmonic generation (SHG)[4] or difference frequency generation (DFG)[5]. The second part passes on without any modification to interfere with the first. The frequency comb is given by

$$f_m = m f_{rep} + f_{ceo}\,, \tag{2.4}$$

and SHG yields

$$2f_m = 2m f_{rep} + 2f_{ceo}\,. \tag{2.5}$$

If the original pulse has a spectrum spanning over an octave, a frequency from the comb f_n satisfies the relation

$$f_n = 2m f_{rep} + f_{ceo}\,, \tag{2.6}$$

where $n = 2m$. The interference between second harmonic and original pulse near the higher end of the frequency comb, results in a beating pattern with a frequency $2f_m - f_n = f_{ceo}$. The resulting beat signal in the form of intensity modulation is detected by a fast photodiode. In case of a DFG process, the same phenomenon occurs, except that the interference takes place at the lower end of the frequency comb with pulses having an offset-frequency of f_{ceo} and 0. The corresponding experimental arrangements to detect f_{ceo} are known as f-to-2f and 0-to-f interferometers, respectively. The determination of CEP by direct detection of f_{ceo} is a very fast and efficient method for active CEP stabilisation and readout.

2.2 Enhanced near-fields in nanotips

An important aspect of using metallic nanotips are the enhanced near-fields formed at the apex during laser irradiation. The near-field refers to the amplified electric field near the tip apex which rapidly decays further away from the apex surface. Due to their higher magnitude as compared to the laser focus, near-fields drive the electron emission from the tip surface. The incident electric fields can be amplified by almost an order, thereby reducing the peak power requirement of the laser [11]. This allows lasers to operate at very high repetition rates leading to much better data acquisition statistics.

They are produced primarily by two mechanisms. One is a purely geometric effect where the electric field of the laser leads to accumulation of charges at the metal-vacuum interface near the tip apex. Depending on the size of the tip apex, a high charge density creates a strong electric field near the apex (shown in Figure 2.3 (b)), and is commonly referred to as the *Lightning rod effect*. This effect applies to a large

[4] A process in which two photons interact with a second order non-linear material to generate one photon with twice the frequency

[5] A process in which one photon with higher frequency and one with lower interact in a second order non-linear material to produce the same photon with lower energy and one with a frequency given by the difference of two

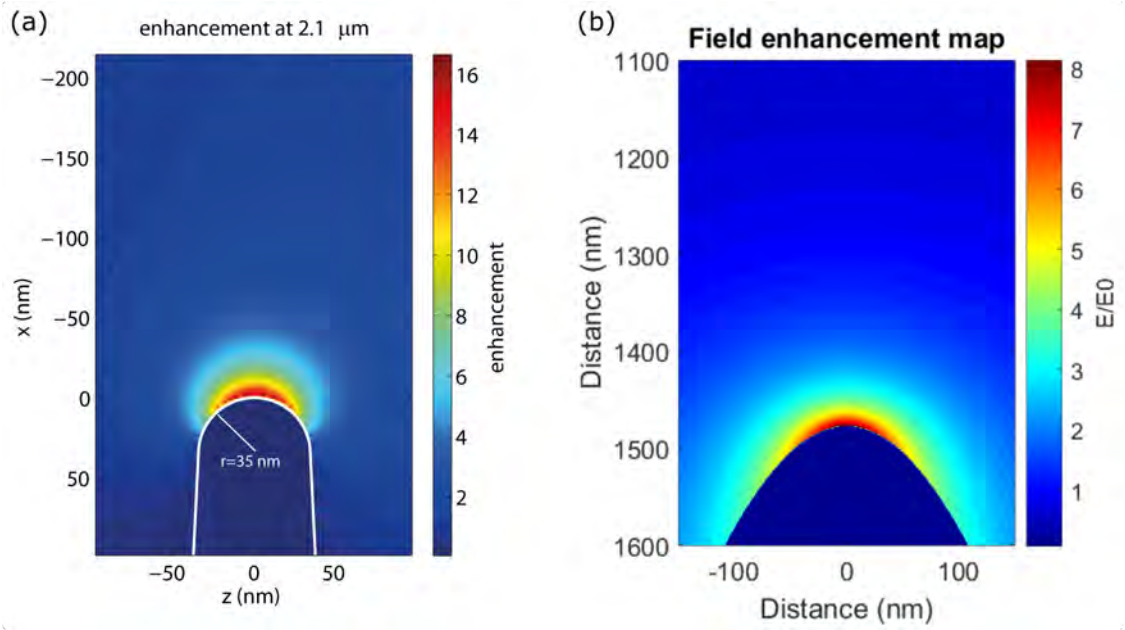

Figure 2.3: **Enhanced fields around gold nanotips.** (a) Finite-difference time-domain (FDTD) simulation of field enhancement on a circular tip shape at a wavelength of 2.1 µm (courtesy of J. Schötz). (b) Simulated field enhancement on a hyperbolic gold tip with a radius of 45 nm by a static-field induced by a counter electrode placed at 0 nm. Here, E_0 has been chosen arbitrarily to reproduce a desired field enhancement. The theoretical model used, does not reproduce the absolute field enhancement accurately (see Section 4.1).

range of tip sizes and wavelengths. The other enhancement effect that occurs, depends on the material and wavelength of the laser along with its geometry. It is caused by excitation of surface plasmons by the oscillating light field. These are coherent electron density oscillations propagating at the metal-vacuum surface of the tip apex, producing a large field enhancement [12]. This effect is significant when there is resonance, which depends on the dielectric constant of the material and wavelength of the laser. The material used in the experiment is gold which exhibits resonance at optical wavelengths due to its negative real permittivity [13]. A detailed theoretical investigation of this effect can be found in a recent work by Thomas et al. [11]. A finite-difference time-domain (FDTD) simulation based on this model is shown in Figure 2.3 (a).

2.3 Laser induced emission dynamics

First studies of electron emission in solids date back to almost a century when Heinrich Hertz' experiment and Albert Einstein's theory gave the world the photoelectric effect. Electrons are photoemitted when they interact with a photon with an energy

higher than the work function of the material. The maximum kinetic energy of these electrons is defined as $E_{kin} = h\nu - \phi$,where $h\nu$ is the energy of the incident photon and ϕ is the work function of the material. It marks a linear regime where the rate of electron emission is proportional to intensity of light.

Later, with the advent of lasers, very high intensities could be reached by means of tight focussing and pulsed operation. This led to the experimental realisation of non-linear photoemission regimes. The regimes are classified based on the intensities where they are predominant and undergo different theoretical treatments. The study carried out in this thesis, spans over both these regimes and is reviewed in this section.

2.3.1 Weak-field regime

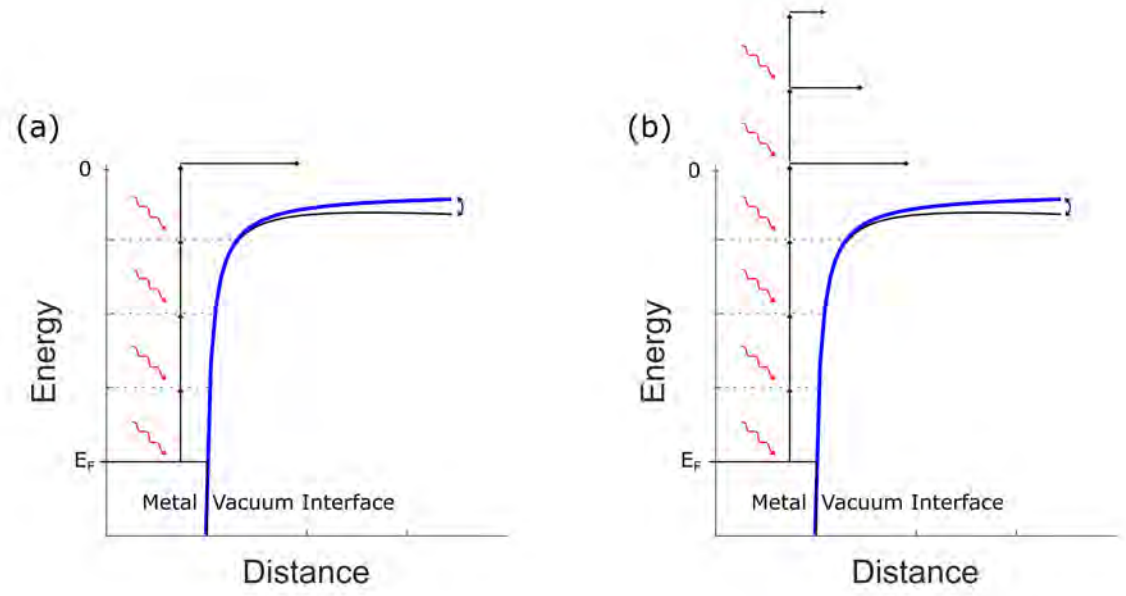

Figure 2.4: **Schematic representation of laser induced photoemission in the multiphoton regime at metal surfaces.** (a) Multiphoton ionization: Here the electrons absorb four photons to exceed the work function of the metal, and are consequently photoemitted. (b) Above-threshold ionization: Along with the multiphoton process, at higher intensities the electrons absorb more photons than necessary, and are emitted at higher energies with discrete energy spacing. This leads to the formation of peaks in the energy spectrum (see Figure 5.2). The blue lines depict the unperturbed barrier potential while the black curves depict the perturbed barrier potential under the action of the laser field. $E_F$is the Fermi energy.

At certain laser intensities, electron emission is primarily governed by multiphoton emission. In this regime, multiple photons are absorbed to emit an electron. When the energy of incident photons is less than the work function ϕ of the material (ionization

energy I_E in gases), an integral number of photons n are absorbed to release an electron over its surface potential barrier. In this case, the maximum kinetic energy of the electrons emitted can be expressed as

$$E_{kin,mpi} = nh\nu - \phi\,. \tag{2.7}$$

The rate of photoionization in this case is given by

$$\Gamma_{LOPT} = \sigma_n I_L^n\,, \tag{2.8}$$

where σ_n and I_L^n are the ionization cross-section and laser intensity respectively for an n^{th} order absorption process. The theory is well understood by treating the laser field as a small perturbation, and is known as the lowest order perturbation theory (LOPT) [14]. According to it, the photon order n is determined by the lowest number of photon energy needed by an electron to be photoemitted over the potential barrier. This regime is valid only up to certain intensities, beyond which the perturbative treatment fails to make accurate predictions.

At an intermediate stage between the two broad regimes, the emission mechanism deviates from the LOPT [15]. This occurs in case of even higher laser intensities where more number of photons are absorbed by the electrons than necessary to overcome the Coulomb potential. This is known as Above-threshold photoemission (ionization in case of atoms) and is schematically shown in Figure 2.4. It manifests itself on the photoelectron energy spectrum in the form of discrete peaks with an energy spacing equal to its photon energy and was first reported in a photoionization experiment with Xenon [16]. The theories of multiphoton processes are well documented and further description can be found in the literature [17, 18].

2.3.2 Strong-field regime

Tunnel Ionization

When the laser fields applied are much higher than in the weak-field regime, the electron emission deviates drastically from the multiphoton behavior. In this case the effect of laser pulses on the surface barrier potential as seen by an electron is no longer a small perturbation but a strong modulation, such that it forms a potential barrier of finite width. This transition from the weak-field behavior can be thought of as a transition from a quantum mechanical 'photon' treatment of light to a classical 'wave' treatment. The strong modulation results in a non-zero probability of the electrons tunneling through the barrier, commonly referred to as tunnel ionization. In contrast to the weak-field regime, the rate of ionization depends on the amplitude of the electric field or instantaneous intensity of the carrier wave within the pulse, instead of the average intensity. This, combined with the very high non-linearity of the process, makes it extremely sensitive to variations in the pulse CEP. It is a widely used tool of disentangling various emission dynamics from pure optical tunneling.

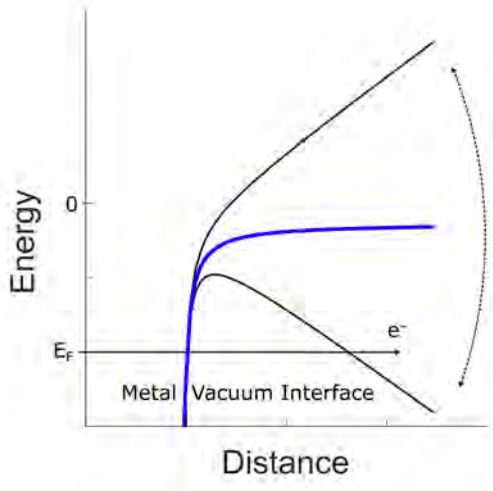

Figure 2.5: **Laser induced tunneling at metal surfaces.** Oscillating laser fields strongly modulate the Coulomb potential as shown in black compared to the unperturbed case in blue. A negative potential barrier slope leads to the formation of a potential barrier of finite width through which electrons can directly tunnel out from its initial state. $E_F$is the Fermi energy.

Our current understanding of the theory for ionization atoms in strong-fields is based on the work of L. V. Keldysh [19] which was extended to metals by the work of Bunkin and Fedorov[20]. The theory uses a non perturbative approach to correctly predict the deviation in the ionization rate when we transit from the weak to strong-field regime. A dimensionless parameter γ, known as the Keldysh parameter is used to distinguish between the two regimes. The parameter is defined as

$$\gamma = \frac{\tau_T}{\tau_L} = \sqrt{\frac{\phi}{2U_p}}\,, \tag{2.9}$$

where τ_T is the quasi-classical tunneling time, τ_L is the time period of field oscillation, ϕ is the work function in case of a metal or ionization potential in the atomic case and U_p is the ponderomotive energy[6], defined as

$$U_p = \frac{e^2 E_L^2}{4m\omega_L^2} = \frac{e^2 I_L}{2c\epsilon_0 m\omega_L^2}\,, \tag{2.10}$$

where E_L and I_L are the electric field strength and intensity of the laser pulse respectively, ω_L is the center frequency of the laser, e is the electron charge, m is the mass of electron, c is the speed of light and ϵ_0 is the vacuum permittivity. Low laser frequencies or high intensities result in a very small Keldysh parameter ($\gamma \ll 1$) leading to the domination of tunnel ionization. The electron tunnels out much quicker

[6]Cycle-averaged kinetic energy of an electron in a laser field

than a change in the field strength (and potential barrier thickness), indicating a static DC-like behavior during the emission interval. On the contrary, in case of very high laser frequencies or low intensities ($\gamma \gg 1$), the ionization is dominated by multiphoton processes. In this case, the electron experiences a time varying surface potential barrier during its emission interval lowering its tunneling probability. The direct proportionality of Keldysh parameter with wavelength makes the use of long-wavelength laser sources ideal for probing into strong-field dynamics. For calculation of the tunnel ionization rate, there are different models which propose relations based on different assumptions. The tunneling rate in a quasi-static approximation ($\gamma \to 0$) is given by the Ammosov-Delone-Karinov (ADK) model [21]. The rate is given as

$$\Gamma_{ADK} \propto \exp(-2(2\phi)^{3/2}/3E)\,, \tag{2.11}$$

where ϕ is the work function and E is the electric field of carrier wave. The exponential dependence on the electric field makes the tunneling rate extremely sensitive to sub-cycle changes in the electric field.

Apart from pure strong-field tunneling, mixed emission processes can also exist. In such cases, the electrons tunnel out after they have been excited by a single or multiple photons. This occurs when the potential barrier at the Fermi level is wide enough to prevent tunneling, but allows it at higher energy levels where the barrier is narrower. This is commonly referred to as photo-field or photo-excited emission and has been reported in laser induced emission experiments in the presence of strong DC bias. [7]

Electron re-scattering

In the strong field regime, the dynamics of the electrons don't just end with its emission into continuum, but are also influenced by the strong electric fields in the laser focus or near-fields in case of nanostructures. The electrons undergo acceleration and according to classical calculations they can gain energies of up to $2U_p$. Laser induced photoemission experiments in gases and more recently in metals have reported electrons of higher energies in the energy spectrum where they form a plateau beyond the $2U_p$ energy of directly accelerated electrons [22, 23].

The emission of electrons, followed by its acceleration in the laser field and eventual re-scattering is commonly referred to as the Three-Step Model [25]. A schematic representation of the three processes in case of atoms is represented in Figure 2.6. The first step, as explained in the previous section is where the electron tunnels out when the potential barrier is strongly modulated. In the second step, the electron exhibits a quiver motion[7] in the presence of an oscillating field. Depending on the birth time of the electron, it can either escape from the binding force of the field or re-scatter with the parent atom or surface. In case of nanostructures, the electrons are primarily influenced by the strong near-fields which decay over a length comparable to the

[7]The wiggle motion experienced by a charged particle in an oscillation electric field

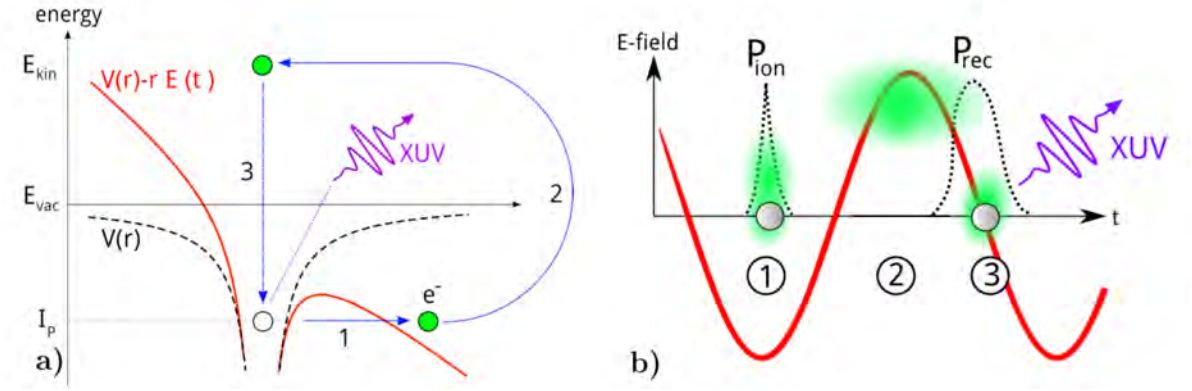

Figure 2.6: **The three step model (TSM) of electron re-scattering in atoms.** [24] (a) Potential energy diagram. (b) Timing of the processes with respect to the incident laser field. Step 1: Tunnel ionization/photoemission of the electron, Step 2: Acceleration in the laser field away and back towards the surface along with the direction of the electric field, Step 3: Re-scattering or recombination with the parent atom with the high harmonic generation of an XUV pulse. The simulated re-scattering process for a metal surface is shown in Figure 4.3.

quiver amplitude[8] of the electron. If the decay length is much smaller than the quiver amplitude, the electron would escape leading to a shift in the expected energy spectrum. This quenching effect has been studied and accounted for by the use of another dimensionless adiabaticity parameter δ [26]. It is defined as

$$\delta = \frac{l_F}{l_q} = \frac{l_F m\omega^2}{eE}\,, \tag{2.12}$$

where l_F is the decay length (1/e) of the enhanced field at the apex, l_q is the quiver amplitude, m is the electronic mass, ω is the central frequency of the laser, e is the electronic charge and E is the effective electric field strength within the near field. When $\delta \gg 1$, the electron gains the complete ponderomotive energy in the field, or it escapes the field before when $\delta \ll 1$. The electrons which are accelerated back can gain maximum energies of up to $3.17U_P$ [27]. In the final step, these electrons can either re-scatter or recombine with the parent atom producing a burst of radiation by high harmonic generation (HHG). In case of elastic re-scattering under non-quenched conditions, the electrons undergo multiple collisions under the influence of the oscillating field, leading to a maximum kinetic energy of [28]

$$E_{max,kin} = 10U_P + 0.538I_P\,, \tag{2.13}$$

where I_P are the ionization potentials, which are replaced by the work function ϕ in case of metals. Unlike the atomic case, the region of elastic re-scattering in metals is

[8]The distance an electron travels under the influence of the oscillating field in one cycle

not so well understood. It is commonly treated as a surface phenomenon but recent studies by Yanagisawa et al. show the possibility of delayed emission by the occurrence of scattering below the surface [29].

In this thesis, the electrons which accelerate in the laser field without undergoing any scattering, are often referred to as direct electrons, and the maximum energy obtained by them is termed as the $2U_P$ cutoff. Similarly, the re-scattered electrons are referred to as indirect electrons, and the maximum energy gained is termed as the $10U_P$ cutoff.

Chapter 3

Experimental methods

This chapter describes the experimental implementation of all the tools required for studying laser induced electron emission from nanotips in the strong-field regime. The laser sources providing ultra-short few-cycle pulses at two different wavelengths are described first. After which, a description of the experimental setup for recording the emission energy spectra are presented. Finally, the fabrication of polycrystalline gold nanotips are briefly described.

3.1 Generation of few cycle laser pulses

The most important tool required for laser induced photoemission experiments is the laser source itself. As discussed in Chapter 2, probing into strong-field emission dynamics which exhibit strong dependence on the electric field evolution of the pulse and not just its average intensity. Hence, it becomes important to have lasers which are capable of producing CEP stable pulses with few electric field cycles. In this section, we describe two laser systems with different central wavelengths that have been used in our photoemission studies.

3.1.1 Few-cycle pulses at 700 nm

Photoemission experiments were carried out with spectrally broad few cycle pulses with a center wavelength[1]around 700 nm. This system generates pulses which are 5 fs long, at a repetition rate of 10 kHz and is schematically represented in Figure 3.1.

The laser pulses are first generated in a mode locked cavity of a commercial titanium sapphire based oscillator (Femtolaser RAINBOW™). In this oscillator, the Ti:Sa[2] is pumped by a frequency doubled diode-pumped Nd:YAG[3] laser (Coherent Verdi). The oscillator cavity is passively mode locked by the Kerr effect and uses sets of chirped

[1]Analogous to center frequency
[2]Titanium-doped sapphire crystal
[3]Neodymium-doped yttrium aluminium garnet crystal

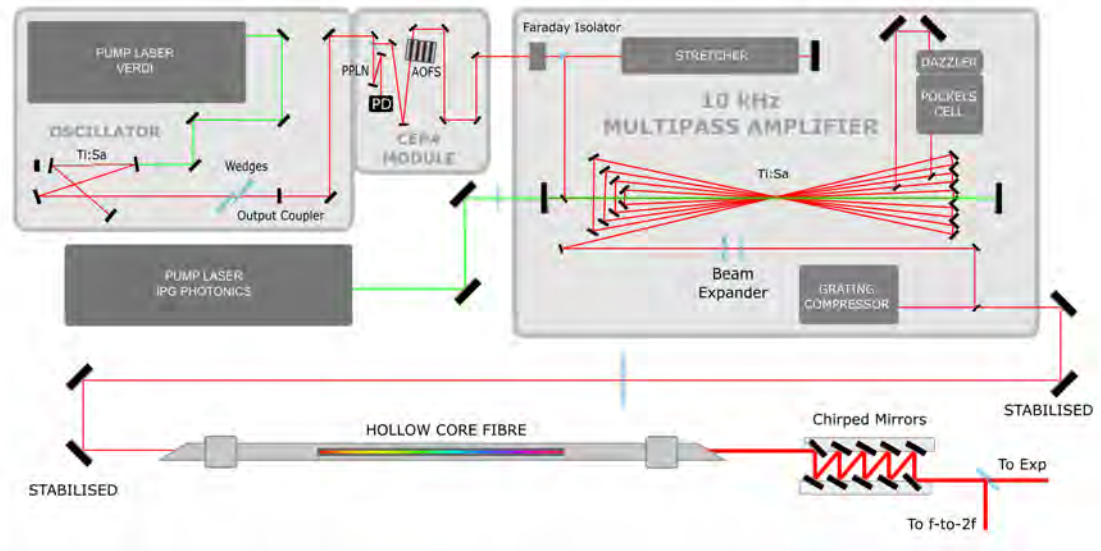

Figure 3.1: **Setup for producing few-cycle laser pulses centered around 700 nm.** Ti:Sa is a Titanium Sapphire crystal, PPLN is a Periodically Poled Lithium Niobate crystal, AOFS is an Acousto-Optic Frequency Shifter, PD is a Photodiode.

mirrors for intra-cavity dispersion compensation [30]. This allows the formation of ultra-short pulses, down to7 fs and pulse energies of up to 6 nJ.

The instabilities in the carrier envelope phase of the laser pulses are corrected by the use of a commercial active phase stabilization module (Femtolaser CEP4™) attached to the oscillator. This module works on the principle of direct feed-forward phase stabilization [31]. The output from the oscillator is fed into this module (CEP4) where it is split in two paths. One gets focused into a PPLN[4] crystal which induces self phase modulation and difference frequency generation [32]. The DFG process produces pulses without the presence of f_{ceo} (offset frequency), while SPM (self-phase modulation) helps broaden the bandwidth of the incident pulse for its successful interference with the latter in the near infrared region. This follows the 0-to-f scheme of self referencing for detecting f_{ceo}, as described earlier in chapter 2. The intensity modulation of the beat signal from the interference is then detected by passing it through a long pass filter and onto a fast InGaAs[5] photodiode. This RF signal generated by the diode is amplified with which it drives an Acousto-Optic Frequency Shifter (AOFS). The second path of the split beam passes through this AOFS where it undergoes diffraction following Bragg's law, but along with a Doppler shift. This causes a shift in the frequency of the outgoing pulse as

$$f_{out} \approx f_{in} + mRF\,, \tag{3.1}$$

where f_{out} and f_{in} are the respective outgoing and incoming laser pulse frequencies,

[4]Periodically Poled Lithium Niobate
[5]Indium Gallium Arsenide

m is the order of diffraction and RF is the detected f_{ceo} applied to the AOFS. Hence, the first order diffraction is used, which shifts the whole frequency comb by f_{ceo}. This allows for fast correction of CEP drifts [31]. The basic processes involved have been schematically represented in Figure 3.2.

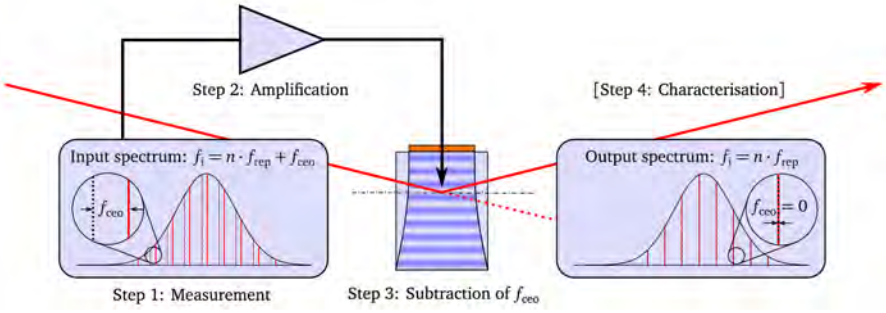

Figure 3.2: **Feed-forward scheme of active CEP stabilisation.** Step 1 and Step 4 shows the frequency domain representation of the laser pulses. Step 3 represents the diffraction of the incoming beam by the use of an Acousto-Optic Frequency Shifter [8].

The laser pulses obtained after the phase stabilisation module are already good enough to produce few-cycle pulses with sufficient energies to carry out laser-induced photoemission experiments on metallic nanotips. Photoemission experiments in gases are also performed to calibrate our system, as described in section 5.1. This requires the use of much higher pulse energies, and it becomes important to use an amplifier along with the oscillator and phase stabilisation module. Apart from that, the laser source is also shared by multiple experiments. Thus, a commercial kHz-repetition rate, multipass Ti:Sa amplifier (Femtolaser FEMTOPOWER™ HR) based on a CPA (chirped pulse amplification) design is used. The amplifier is seeded by the output of the phase stabilisation module. In the first step, the ultra-short seed pulses are stretched by passing them through glass. This reduces the peak intensity of the pulses, allowing amplification without damaging the gain medium, which is a Ti:Sa crystal optically pumped by a frequency doubled Q-switched Nd:YAG laser. After the seed pulses have traversed four passes through the gain medium at a repetition rate of the oscillator (75 MHz), they pass through a pockels cell where their repetition rate is reduced to 10 kHz. At this stage, the pulses undergo compensation of the third and fourth order dispersion, by the use of an acousto-optic programmable dispersive filter (Fastlite DAZZLER) [33]. The pulses are further amplified by making five more passes through the gain medium and they finally leave the amplifier after undergoing compression by a grating compressor. The pulses obtained from the amplifier are 25 fs long and cannot be compressed further as their bandwidth is reduced by gain-narrowing in the amplification process [34].

To compress the pulses further, the bandwidth needs to be broadened. This is achieved when the pulses pass through a gas-filled hollow core fiber. The laser beam is

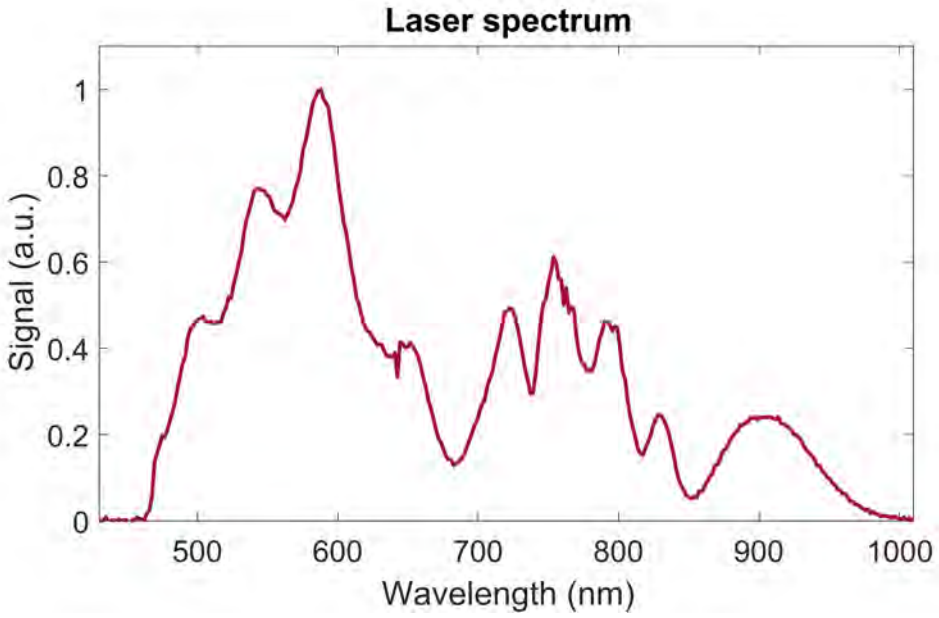

Figure 3.3: **Measured laser spectrum after the hollow core fiber.**

coupled into the fiber by focusing it with a long-focus lens in the gas, leading to SPM and spectral broadening [35]. In our case, the fiber is 1 m long with a 250 µm core filled with Argon. Given the aspect-ratio of the fiber core, it becomes quite important to be very precise with the alignment of the in-coupling beam. Small deviations in the beam propagation direction lead to large fluctuations in power and spectrum of the output from the fiber. Thus, to guide the beam from the amplifier to the fiber, we use a pair of mirrors fitted with active beam stabilisation which compensates for all such deviations. Finally, the pulses are compressed by compensating for the positive chirp induced by SPM in the fiber core by pairs of negatively chirped multilayer mirrors [35, 30]. The amount of negative dispersion induced is decided by also taking into account the positive dispersion acquired by the pulses before they actually reach the experiment. A pair of fused silica wedges are used to fine tune the chirp such that we obtain chirp-free pulses at the experiment. Finally, we obtain pulses which are 5 fs long (measured using a FROG[6] setup) and with pulse energies of up to 100 µJ.

The beam is then split up in two. One goes to our photoemission experimental chamber and the other travels to an f-to-2f interferometer setup for reading out the carrier envelope phase. This works on the f-to-2f scheme of self referencing as described earlier in the second chapter.

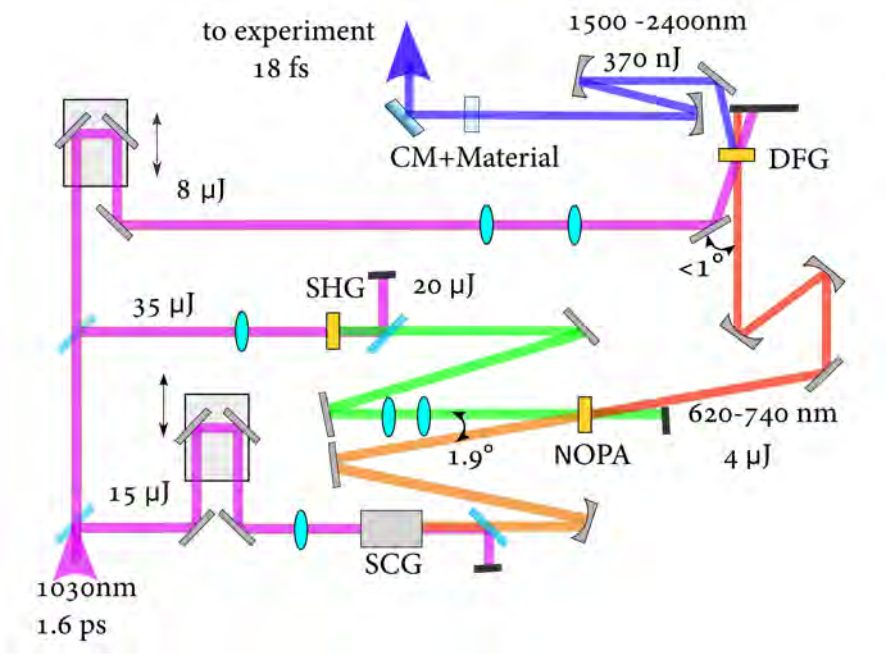

Figure 3.4: **Setup for generating few-cycle pulses centered at 1800 nm.** SCG is super continuum generation, SHG is second harmonic generation, NOPA is noncollinear optical parametric amplification, DFG is difference frequency generation and CM are chirped mirrors (Courtesy of Marcel Neuhaus).

3.1.2 Few-cycle pulses at 1800 nm

As described in the previous chapter, an inherent requirement for studying strong-field physics is working in a regime where the Kelsysh parameter is very small ($\gamma \ll 1$). To achieve this, we need to increase the ponderomotive energy U_P (see Equation 2.9), which in turn is directly proportional to the wavelength squared (see Equation 2.10). Thus, by using longer wavelengths, we can significantly affect the Keldysh parameter, and hence scale the emission dynamics towards the optical field or tunneling regime [36]. A common way to achieve this is by the use of a broadband Ti:Sa based laser systems and use a parametric amplification process to amplify certain wavelengths [37]. As these measurements require very good statistics, we need to use high repetition rate lasers leading to very high average-power requirements. This is one of the primary limitations of a Ti:Sa based parametric amplification setup. Although this is not a problem for carrying out measurements with metallic nanostructures [26] due to its field enhancement, we need an alternative for experiments with gases. Given the added advantages, a part of the Kling group has developed a system based on Yb:YAG[7] [38] and many of the results discussed in this thesis are some of the first experiments carried

[6]Frequency resolved optical gating
[7]Ytterbium-doped yttrium aluminum garnet crystal

out with it. In this section, we briefly describe the setup and properties of the system.

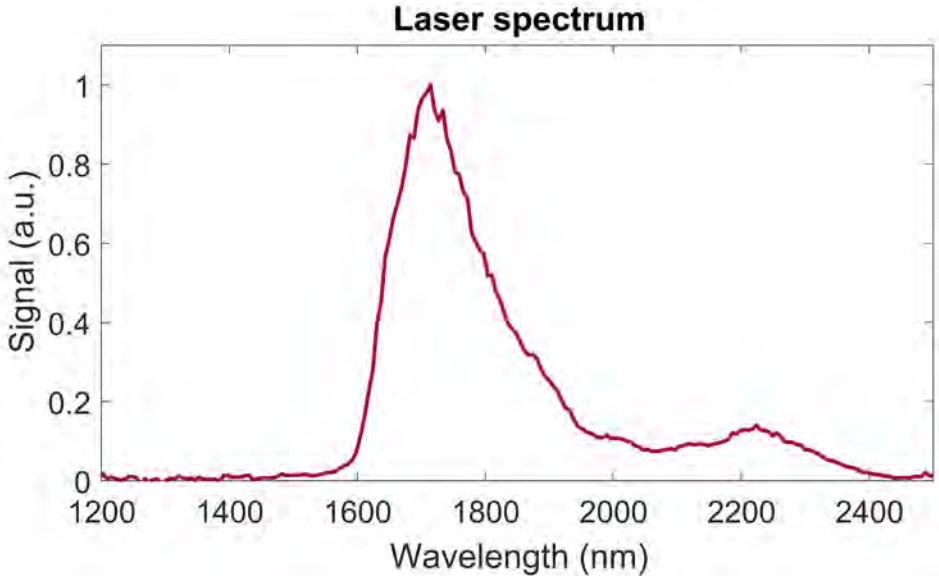

Figure 3.5: **Measured spectrum of the 1800 nm laser source (center wavelength)**

The laser is based on a chirped pulse amplification system with a multi-pass Innoslab amplification configuration developed at the Frauhofer-Institute for Laser Technology, Aachen, Germany. The system generates pulses centered at 1030 nm with a pulse duration of 1.6 ps, operating at 100 kHz and is capable of producing up to 400 W of output power. These pulses seed the setup for parametric amplification of the desired wavelengths as shown in Figure 3.4. Here the beam is split in three parts. One is used to generate white light by super continuum generation (SCG) in a YAG crystal [39] which serves as a seed for the noncollinear optical parametric amplifier (NOPA). The second part of the beam from the Innoslab is focussed in a Barium borate crystal (BBO) to produce the second harmonic, which in-turn serves as a pump for the NOPA. Parametric amplification of the white light is achieved in the NOPA, and its output is used to pump the difference frequency generation (DFG) process. Finally, the third part of the output from the Innoslab undergoes DFG with the output from the NOPA to produce a broad spectrum output centered at 1800 nm with pulse energies of 370 nJ. The pulses are further compressed by passing them through sapphire plates and chirped mirrors to produce pulses with the duration of 18 fs, as measured by a FROG setup. In theory, this is quite close to a few cycle configuration (see Figure 2.1 (b)).The CEP stability of the pulses were also measured using an f-to-2f interferometer. Although there were some short term fluctuations, the CEP was observed to be suitably stable over a long period. This is also seconded by the possible observation of ATI peaks in the photoelectron spectrum from gas, discussed later.

3.2 Measurement of photoemission energy spectra

In this section, we present a brief overview of our experimental chamber and the various techniques involved in carrying out laser induced photoemission experiments on gold nanotips.

3.2.1 Experimental chamber

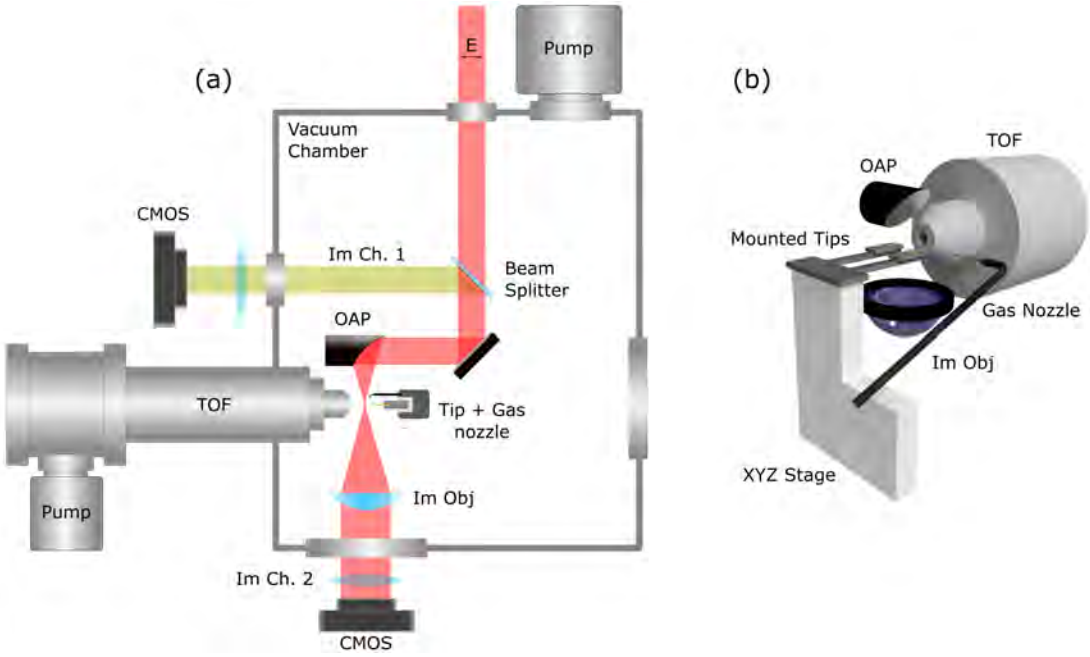

Figure 3.6: **Experimental setup for laser induced photoemission experiments.** a) Vacuum chamber. b) 3D close-up view of photoemission region. TOF is an electron Time Of Flight spectrometer, OAP is an Off-Axis Parabolic mirror, Im Ch. are Imaging Channels and Im Obj is an Imaging Objective.

The essential components of the photoemission setup are placed inside a vacuum chamber as depicted in Figure 3.6 (a). The chamber is designed for high-vacuum applications where we obtained pressures down to 10^{-7} mbar. Electron photoemission experiments cannot be performed under atmospheric conditions given the short mean free path of electrons. Good vacuum conditions are also desired to prevent contamination of the nanotip surface. We use a differential pumping system comprising a pre-pump (10^{-3} mbar) and two turbo pumps (Pfeiffer Vacuum). The laser beam enters the chamber through a window which is made of fused silica when used with 700 nm pulses and sapphire with 1800 nm pulses. The beam then goes through a beamsplitter and finally on to a tight-focussing silver off-axis parabolic mirror (OAP) with a focal

length of 15 mm. The beam waists of the foci were measured as 2.1 µm[8] and 2.6 µm[9] for the 700 nm and 1800 nm laser pulses, respectively.The nanotips are positioned in the focus, parallel to the polarisation of the electric field. Here, tight focussing reduces the laser irradiation area on the nanotips, restricting it to the tip apex. The nanotip itself is placed on a metal sheet which is insulated from the whole chamber by a ceramic holder and is connected to a voltage supply channel via a vacuum feed-through. This channel is normally kept at 0 Volts during our measurement. However, before the measurement, we apply a small bias to check for correct grounding by looking at the photoelectron energies. The tips along with the ceramic holder are placed on a XYZ motorized stage (SmarAct Linear Positioners) with a minimum step size of 50 nm. To prevent opening the chamber very often, we mount up to three tips at the same time. This arrangement is closely shown in Figure 3.6 (b).

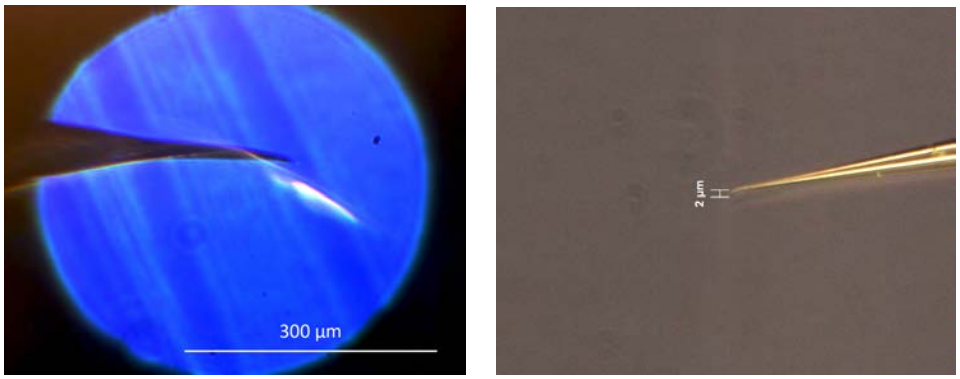

(a) (b)

Figure 3.7: **In-situ microscopy for visual feedback.** (a) Image of a gold nanotip on a CMOS sensor, captured using the Off-axis parabolic mirror as the objective. (b) Image of a similar nanotip captured by a high-end commercial light microscope (Zeiss).

After the laser focus, the beam diverges and is collected by a plano-convex lens with a focal length of 25.4 mm. This lens acts as an objective for a microscope setup described in Figure 3.6 (a) as Imaging channel two. The microscope magnifies and re-images the laser focus on to a CMOS/CCD sensor. We use this to approximately characterize the size of the laser focus with the 700 nm laser. We use another microscope setup as another Imaging channel (channel one), which uses the OAP itself to image the focal region. As shown in Figure 3.7 (a), we use an external visible light source to illuminate the background such that the nanotip casts a shadow, which is imaged by a CMOS sensor. The beamsplitter shown in the setup is used to separate the laser beam and the imaging beam paths as shown in the setup. By this method, in case

[8]Measured using the magnified image of the laser focus on a CMOS sensor using imaging channel 2, as shown in Figure 3.6 (a)

[9]Measured using a knife-edge setup

of a visible laser beam, we can also image the laser scatter off the tip surface. This saves a lot of time spent otherwise on the coarse alignment of the nanotip in the laser focus. However, the final alignment is done carefully by maximizing the electron yield registered by the time of flight spectrometer.

Another important aspect of this setup is the presence of a gas nozzle, as depicted in Figure 3.6 (b). As the strong-field photoemission dynamics in gas are very well studied, we use it to calibrate our measurements. This will be explained in greater detail in a later chapter. The nozzle is fabricated in the lab from hollow core glass fibers of specified diameter. In our case this was a 100 µm fiber with a 10 µm core. After which, they are coated with graphite and grounded to avoid charging effects during laser irradiation. In our experiments, we use Argon and Xenon.

3.2.2 Data acquisition

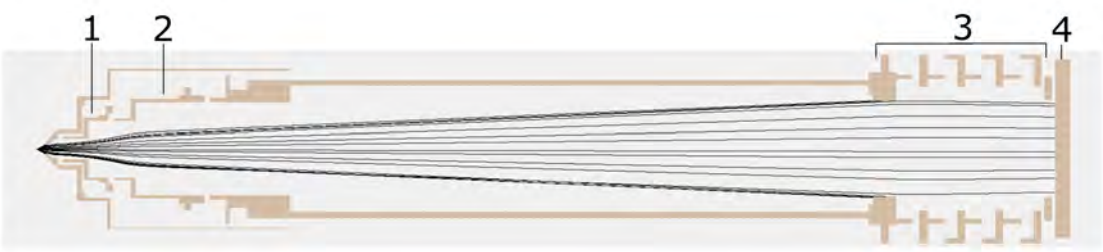

Figure 3.8: **Lateral section of the time of flight spectrometer.** The trajectories of emitted photoelectrons are represented as black lines. (1)Lens electrode (100 V), (2) Drift tube electrode (0 V), (3) Post acceleration electrodes (2.6 kV) and (4) is Microchannel plate detector. The values in brackets indicate the configuration for this specific trajectory simulation.

The primary observable in our experiment is the energy resolved statistics of the electrons photoemitted from the gold nanotip. To measure this, we use a commercial time of flight spectrometer (Käsdorf ETF10). As represented in Figure 3.8, the electrons drift along the tube of the spectrometer until it generates a signal on a microchannel plate detector (MCP) at the end of the tube. It is equipped with three sets of electrodes where the lens electrodes are used to increase the collection efficiency by leading electrons with higher divergence angles on to the MCP while the drift tube electrodes form a high pass energy filter. Due to problems with energy calibration in presence of finite lens and drift tube voltages, they were always kept at zero potential during the measurements. Given the position of the laser focus with respect to the TOF entrance, the maximum acceptance angle turns out to be 6°. The post acceleration electrodes are supplied with potentials of up to 2.6 kV, and are used to increase the detection efficiency of the MCP.

This spectrometer records the time it takes for the electrons to reach the MCP,

thereby generating time of flight spectra. This done by the use of an ultrafast multiscaler (FAST ComTec P7889) with a time resolution of 100 ps. The time of flight spectra are then converted to its corresponding energy spectra using the calibration curves provided by the TOF manufacturer. The calibration curves are based on finding the kinetic energy of the charged particle, given the time it takes to travel a certain distance. Having all the electrodes at ground potential, it can be simply defined as

$$E_{kin} \approx \frac{1}{2} m \frac{l^2}{(T)^2}\,, \tag{3.2}$$

where m is the mass of the charged particle, l is the length of the free drift region of the TOF and $T = t_e - t_p$ is the difference in time of arrival of the electron t_e to that of the laser pulse t_p as recorded by the MCP. The energy resolution is then given by

$$\frac{\Delta E}{E} \approx \frac{2\Delta l}{l} + \frac{2\Delta T}{T}\,. \tag{3.3}$$

Here, we observe that for a fixed TOF length and time resolution, the energy resolution decreases as we have electrons with higher energies. The configuration of our TOF resolves well the electron energies in the range as expected from our experiments. This results in a photoelectron spectrum (see Figure 5.1) with the statistics of the electron counts in each energy bin. For better visibility of the spectral features, we use a log scale on the Y axis.

We also perform CEP resolved measurements with the 700 nm laser. The oscillator in this system is equipped with a pair of silica wedges (see in Figure 3.1) placed on a motorized stage which is scanned linearly (triangular wave) to sweep the phase of the pulses. The change in CEP is detected by the f-to-2f interferometer setup placed after the hollow-core fiber which feeds this information to a computer. We split the phase range of $0 - 2\pi$ in twenty phase bins and use a program to phase tag the corresponding data from the TOF. The energy spectrum is obtained by carrying out a weighted average over all the phase bins. Two common methods of plotting the phase resolved data are as in the form of a Phase map and an Asymmetry map. The phase map is a 2D color map of twenty (doubled to forty for better visibility) phase bins, which include the energy spectra recorded in each phase bin. However, the CEP varying effects are not so clearly resolved. Thus, we use another plot called the asymmetry map. To compute this map, we use an asymmetry parameter defined as

$$A(E_{kin}, CEP) = \frac{S(E_{kin}, CEP) - S(E_{kin}, CEP + \pi)}{S(E_{kin}, CEP) + S(E_{kin}, CEP + \pi) + \epsilon}\,, \tag{3.4}$$

where the parameter $A(E_{kin,}CEP)$ is a function of the kinetic energy and and the CEP. S refers to a particular energy spectrum at a specific CEP and ϵ is a small number to avoid division by zero. Intuitively, the asymmetry parameter measures the deviation of the electron yield at a specific energy and phase, to its counterpart, π phase away.

3.3 Nanotip fabrication

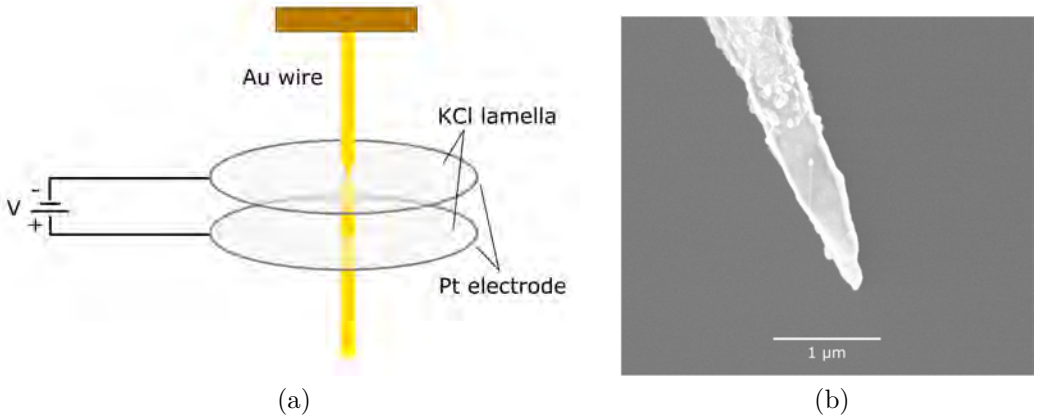

(a) (b)

Figure 3.9: **Gold nanotip fabrication.** (a) Schematic representation of a double lamellae based electro-chemical etching setup [40]. (b) SEM image of a gold nanotip used in our experiements.

In our experiment we use gold nanotips with tip radius' ranging from 25 to 50 nm. The use of gold is quite beneficial owing to its relatively high thermal capacity and plasmonic nature. These are produced by the group of Peter Hommelhoff using a modified lamella drop off technique developed in their group [41]. Here, they use KCl[10] as an etchant, which was verified to produce tips of high surface quality with minimal contamination on gold. The basic principle of operation is that the etchant is applied on a gold wire in the form of a thin lamella which comes in contact with the poly-crystalline gold wire hung from a support. The lamella is formed on a platinum ring electrode when it is taken out after being completely submerged in KCl. As shown in Figure 3.9 (a), two such lamella electrodes are used. Etching is done by the upper lamella (negative polarity), while the lower one is used just to complete the DC circuit. The advantage of such an arrangement is that the current flowing through the etching region is immediately switched-off after the detachment of the lower half of the wire. This makes sure that the etching process does not last beyond the detachment of the tip.

[10]Potassium Chloride

Chapter 4

Numerical methods

This chapter describes the implementation of a simple numerical model for simulating electron emission from nanotips by few-cycle pulses. It is implemented in two dimensions and is based on the well established three step model in a quasi-static approximation, that has been used in similar studies [26, 42]. In this thesis, it has been remodeled to match our experimental specifications, to better understand the electron propagation effects in the nanotip's near field. The simulations are focussed on emission dynamics with 1800 nm laser pulses, where there are strong indications of emission taking place in the strong-field regime.

4.1 Description of the model

The model is categorized in three parts. The electric field which defines the near-field around the nanotip for the given tip specification, the probability of electron emission by tunneling in time and space, and finally its propagation in the field.

Electric field

In the first step, the near-field around nanotip is modeled. This can be calculated very accurately by solving Maxwell's equations numerically [11, 43], but this remains a time consuming and computationally heavy approach. Its is especially challenging to model curved surfaces accurately by this approach. Instead, a much simpler approach is chosen where only geometric effects are considered (see Section 2.2). In this approach, a hyperbolic tip shape is chosen which has been shown to produce results in close agreement with experimental studies [44]. They also provide an analytical solution to derive the near field at the tip in a quasi-static approximation. This is similar to having a static potential distribution around the tip induced by a semi-infinite counter electrode. Instead of a counter electrode, this idea can be extended to having a time-varying optical-field (polarized parallel to the tip axis) inducing a time-varying

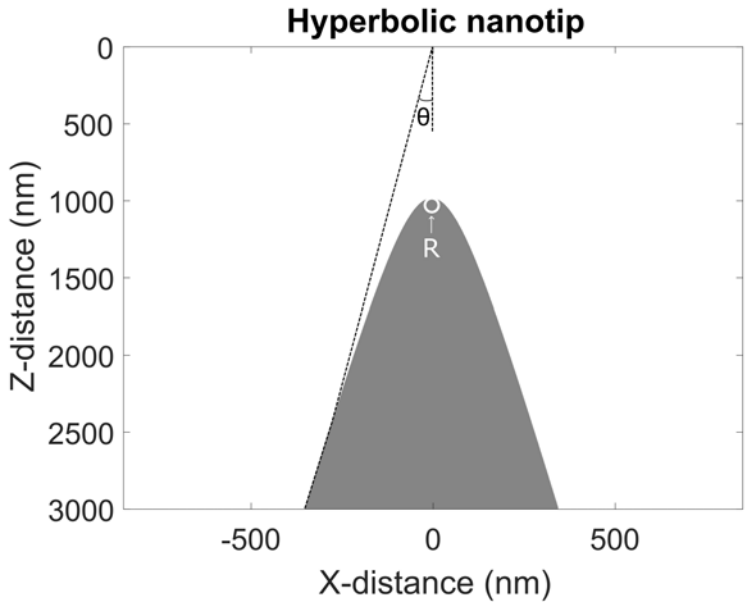

Figure 4.1: **Nanotip geometry.** Computed structure of the hyperbolic nanotip on Cartesian coordinates, showing the two defining parameters, radius R and tip shank angle θ. The counter electrode is assumed to be placed at $z = 0$.

potential[1] around the tip apex. The potential is given by an analytical solution. It is obtained by solving the Laplace equation $\Delta V = 0$, where V is the electrostatic potential. A general solution is obtained in the prolate spheroidal coordinate system [45] and in our specific case, derived as [44, 46]

$$V_I = V_0 P_v(\alpha) P_v(\beta)\,, \tag{4.1}$$

$$V_{II} = V_0 (a P_v(\alpha) + b P_v(-\alpha)) P_v(\beta)\,, \tag{4.2}$$

$$V_{III} = V_0 c P_v(\alpha) P_v(\beta)\,, \tag{4.3}$$

for the three different regions: the tip (I), vacuum in between the tip and surface (II) and semi-infinite counter electrode (III). Here, P is a Legendre function of the first kind with degree v, V_0 is a scaling factor and α, β are the coordinates in prolate spheroidal coordinates. α and β are chosen as the coordinates over the more generally used η and ξ [45] where $\alpha = \cos(\eta)$ and $\beta = \cosh(\xi)$ and should not be confused with the latter. The potentials are defined assuming a rotationally symmetric hyperboloid tip geometry with an apex radius R and the apex half opening angle θ (see Figure 4.1). The spheroidal coordinates are interchanged with 2D Cartesian coordinates x and z whenever necessary using the following transformations

$$x = k\sqrt{(\beta^2 - 1)(1 - \alpha^2)}\,, \tag{4.4}$$

[1] Retardation effects are neglected

$$z = k\alpha\beta\,, \tag{4.5}$$

$$\alpha = \cos\left(Im\left(\cosh^{-1}\left(\frac{z+ix}{k}\right)\right)\right)\,, \tag{4.6}$$

$$\beta = \cosh\left(Re\left(\cosh^{-1}\left(\frac{z+ix}{k}\right)\right)\right)\,, \tag{4.7}$$

where k is a scaling factor. The tip is defined by $\alpha = \alpha_0$, and counter electrode surface by $\alpha = 0$. Then, the apex radius, half opening angle and the tip-electrode surface distance can be configured by the scaling factor k and α_0 as

$$R = k\alpha_0\left(\frac{1}{\alpha_0^2} - 1\right)\,, \tag{4.8}$$

$$\theta = \cos^{-1}(\alpha_0)\,, \tag{4.9}$$

$$d = k\alpha_0\,, \tag{4.10}$$

respectively. Having a specific configuration defined, the degree of the Legendre function v, and constants a, b, c used in the potential function are computed by solving the four boundary conditions at the tip-vacuum and vacuum-surface interfaces. The boundary conditions include the frequency dependent complex dielectric constants $\tilde{\epsilon_1}$, $\tilde{\epsilon_2}$ and $\tilde{\epsilon_3}$ of the respective media. One of the boundary conditions gives the degree of the Legendre function v, which turns out to be a complex value. For the chosen dielectric constants [2], the complex part of the degree contributes negligibly and is ignored to increase computation speed. Under these assumptions, the Legendre functions were computed using a real valued Gauss hypergeometric function. Once the potential is known, the corresponding electric field $\vec{E_{tip}}(x,z)$ is computed by taking its negative gradient. This modeling is carried out to compute the field enhancement produced near the tip apex. Thus, a scaling factor E_0 is chosen such that the peak field enhancement is close to an expected value (see Figure 2.3) and it gives us a function for the enhanced field $\vec{E}_0(x,z)$. The time varying optical field is reproduced by using the electric field evolution of the few-cycle laser pulse (see Equation 2.1) and the enhanced field $\vec{E}_0(x,z)$. The final form of the time varying electric field can be written as

$$\vec{E}(x,z,t) = \vec{E}_0(x,z)\cdot e^{-2\ln 2\frac{t^2}{\tau^2}}\cos(\omega_0 t - \varphi)\,, \tag{4.11}$$

where t is the elapsed time, which runs from the time of birth of an electron, to the end of the pulse duration. All the other variables have their usual meaning as described before.

[2] $\epsilon_1 = -131.21 + 16.658i$, $\epsilon_2 = 1$, $\epsilon_3 = \epsilon_1$

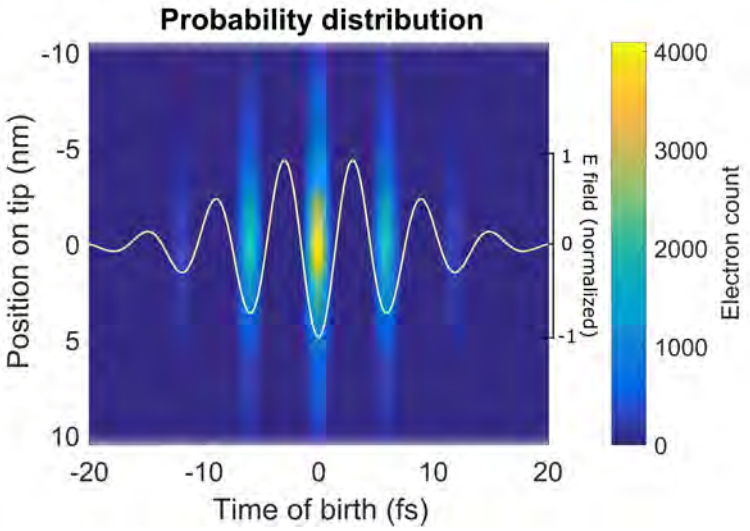

Figure 4.2: Probability distribution of electron emission over time and space. The X axis represents the spatial position on the tip surface and the Y axis represents the time of birth with respect to the laser field as shown in white. This distribution was calculated for a tip with a radius of 3 nm, and a 18 fs laser pulse at 1800 nm. The color bar shows the number of electrons generated at each position and time.

Emission

The probability of electron emission $p(x, z, t)$ in the tunneling approximation is taken into account using a Fowler-Nordheim relation, given as

$$p(x,z,t) \propto \Theta\left(\vec{E}(x,z,t)\right) |\vec{E}(x,z,t)|^2 \exp\left(-\frac{4\sqrt{2m\phi^{3/2}}}{3\hbar e|\vec{E}(x,z,t)|}\right), \tag{4.12}$$

where ϕ is the work function of the tip and Θ is the Heaviside step function to account for electron emission only during negative field cycles. This is due to symmetry breaking at the metal surface. The probability distribution is given as a function of the electric field strength at time t, and the position x, z on the tip apex. The electrons are generated at positions and time with a non-zero probability of emission (see Figure 4.2).

Propagation

After emission, the electron trajectories in the laser field are simulated in two dimensions using the equations of motion

$$m\ddot{x}(t) = -eE_x(x,z,t)\,, \tag{4.13}$$

$$m\ddot{z}(t) = -eE_z(x,z,t)\,, \tag{4.14}$$

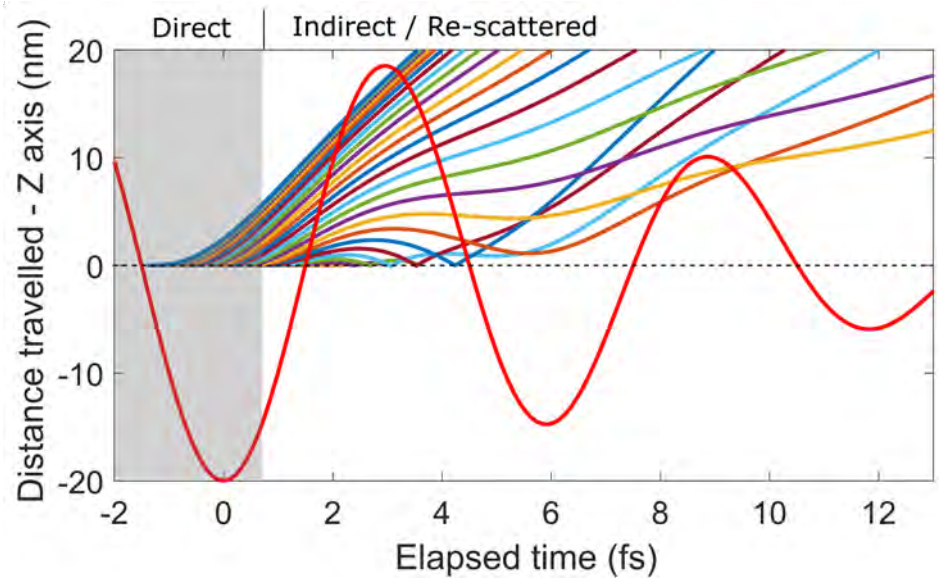

Figure 4.3: **Simulated electron trajectories (1D) in laser field.** The plot considers electrons emitted only during the negative central field cycle. The electric field evolution of the laser pulse is shown in red and the electrons are shown in other colors. Depending on the birth time of the electrons, they either escape the field without re-scattering (direct electrons) with the surface (z=0) or they collide and are back scattered (indirect / re-scattered electrons). Time zero indicates the time at which the laser field reaches a peak negative value.

where m is the electronic mass and e is the electronic charge (see Figure 4.3). They are numerically integrated, using a non-adaptive fourth order Runge-Kutta method with a step size $\leq 1/200^{th}$ of a field cycle. The electrons which are accelerated back to the tip surface are assumed to undergo perfectly elastic collisions with a probability of one. The kinetic energies are recorded from the terminal velocities once the laser pulse is over.

Finally, the photo-electron spectrum of the electron energies for a given laser pulse, are calculated for comparison with the experimental data. This is done by averaging over the final kinetic energies of all the electrons weighted by their probability distribution function. A more rigorous approach would be to use Monte-Carlo methods like inverse transform sampling from the probability distribution function.

The simulations have been performed using this model both in 1D and 2D. Additionally, a few simulations were also performed using a 1D model with the near-field approximated as an exponentially decreasing function with a custom defined decay length. These were generously provided by Johannes Schötz and is referred to in the thesis as 1D-exp, while the other are referred as 1D and 2D respectively.

4.2 Simulations

Emission from a 70 nm tip

In the strong-field regime, observing how electrons accelerate in near-fields, is important for understanding underlying features in the photoelectron spectrum. Here, we simulate our model based on a 70 nm tip with a relatively large near-field decay length. We do not expect any quenching effects at such large decay length's. Looking at the final kinetic energy of the electrons as a function of its emission time with respect to the laser pulse evolution, proves to be quite intuitive in understanding the photoelectron spectra (see Figure 4.4). As shown in the referred figure, the photoelectron spectrum observed using a time of flight spectrometer is a projection of final kinetic energy of the electrons in each cycle. The electrons which are emitted earlier in the laser cycle, quiver in the field without scattering off the tip surface. This is shown in the shaded region of Figure 4.3 and 4.4 (c) and are also referred to as direct electrons. The electrons which gain maximum energy without scattering define the cutoff energy ($2U_P$) for direct electrons. Some electrons travel towards the tip with a large momentum which is not overcome by the opposing field. This leads to elastic scattering at the tip surface and they continue their quiver motion after re-collision. These are referred as indirect electrons. The final kinetic energy gained are much higher as they start from the tip surface with an initial momentum in the forward direction (away from the tip). The highest energies achieved, are by the electrons emitted in the first few field cycles as they quiver in the subsequent cycles for a longer time. This is also evident from the simulations. The signature of these processes can observed on the photoelectron spectrum (see Figure 4.4). The final kinetic energy plot consists of evenly distributed

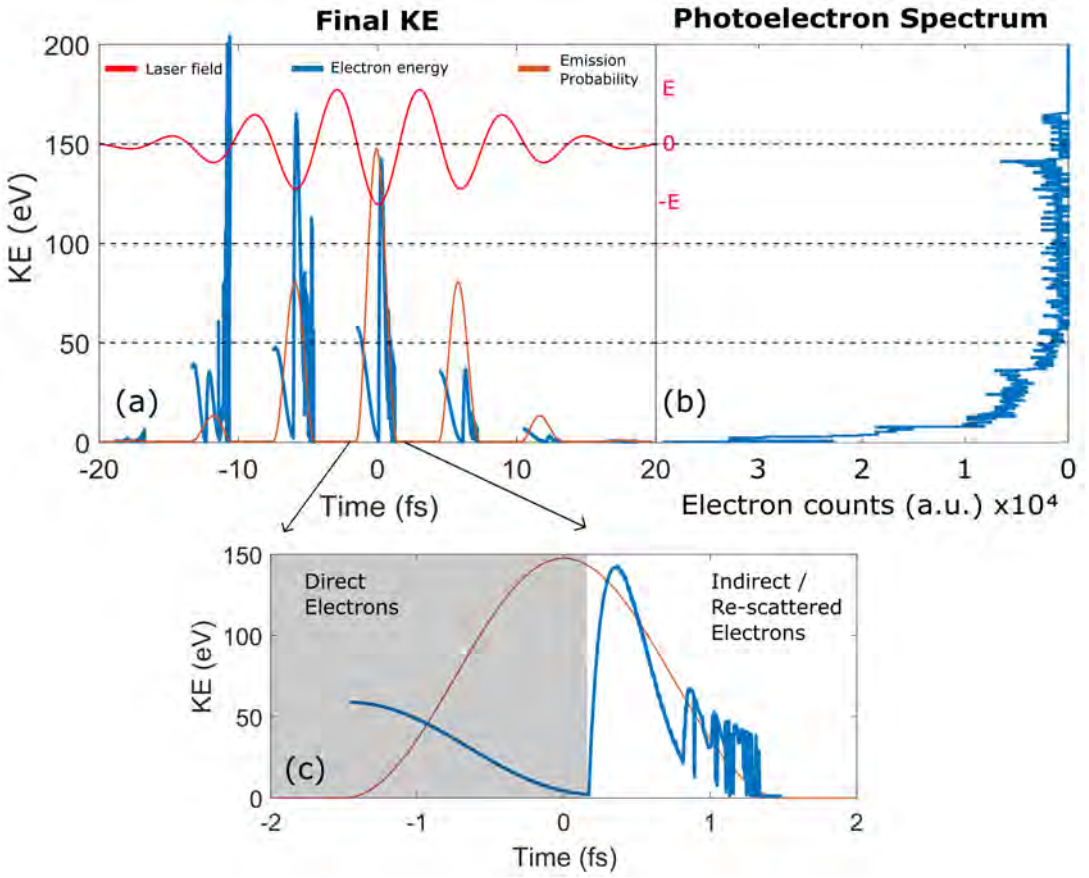

Figure 4.4: **Generation of photoelectron spectrum from the final kinetic energy of electrons (1D).** Plot (a) shows the final kinetic energy of the electrons against the time at which they are emitted from the surface of the tip with respect to the laser field. Plot (b) is the photoelectron spectrum which shows the total electron yield at each energy bin from their final kinetic energies, weighed with their respective emission probability. Plot (c) closely shows the emission at the peak cycle of the laser field. Here, the gray shaded area represents the region where the electrons directly escape from the enhanced fields away from the tip surface, while the non-shaded region corresponding to electrons which are back accelerated and undergo elastic scattering. These were simulated using 1800 nm laser pulses with an incident intensity of 1×10^{12} W/cm^2 with an assumed peak field enhancement of 8. The hyperbolic gold nanotip was assigned a radius of 70 nm, to closely reproduce the tip structure used in experiments.

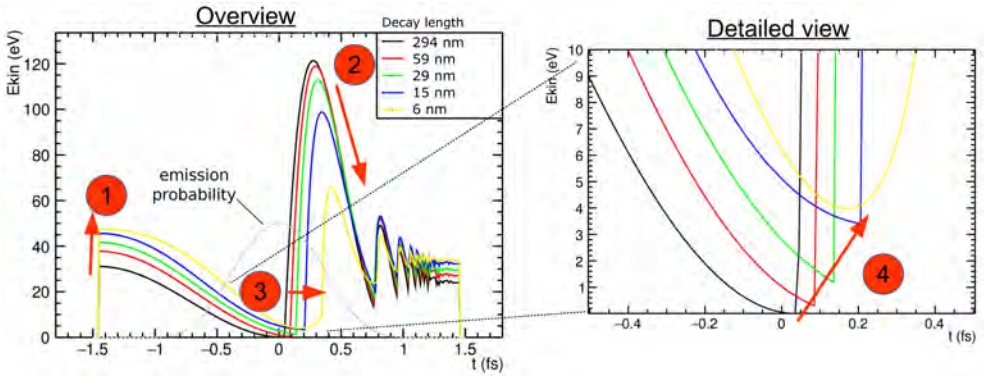

Figure 4.5: **Near-field decay length dependence of final kinetic energies (1D-exp).** Consequences of reducing the decay length: (1) Direct electrons gain higher energy, (2) Maximum energy gained by re-scattering is reduced, (3) Re-scattered electrons are pushed towards later emission times, reducing the emission probability, (4) the low energy cutoff increases in energy. (Courtesy of J Schötz)

electrons over the time axis, and the number of electron counts binned on the energy axis is inversely proportional to the absolute slope of the curve. This leads to formation of peak structure whenever the slope becomes zero at the turning points in the curve. It is especially prominent at the transition region between the direct and indirect electrons as the slope is small over large emission times. The re-scattered part forms steeper slopes leading to more even distributions of electron count. This forms the re-scattering plateau.

Emission from a 3 nm tip

The experimental data obtained with 1800 nm laser pulses (see Section 5.2.2) shows signs of a shifted low energy peak. This unlike the simulated spectrum in Figure 4.4 (b), peak at energies between 0.5-1.5 eV with a clear falling edge on both sides. Also, the re-scattering plateau does not exhibit a very clear cutoff. Simulations in 1D-exp (see Figure 4.5) reveal that the decay length of near-fields at the nanotip apex affects this peak position and suppresses re-scattering. To investigate this, intensity varying simulations are carried out using 1D and 2D models with an exaggerated small decay length. In the used model, the decay length is reduced by modeling a smaller the tip size (≈3 nm). The decay length is ca. 2.5 nm, and operating in a regime where the electrons experience quenched motion. As a comparison, the decay length for the experimentally matching tip specification was about 60 nm.

The intensity varying 1D simulations are shown in Figure 4.6. As expected, a strong suppression of re-scattered electron energies are observed. This aspect is explained by the quenching of quiver motion of electrons. As a result, the electrons scatter with smaller velocities leading to lower final kinetic energies. They also shift towards later emission times reducing its contribution on the photoelectron spectrum. Another

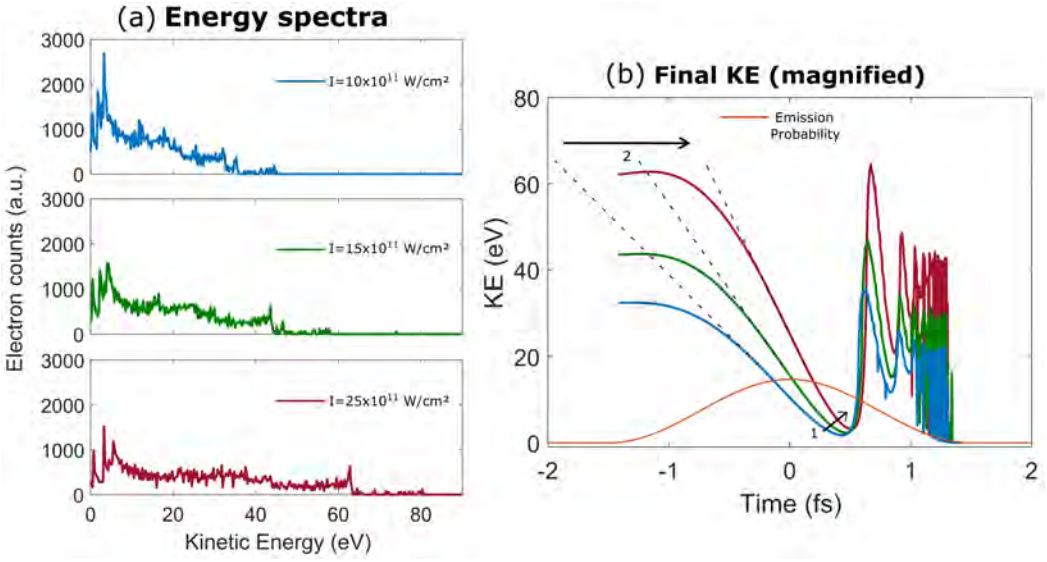

Figure 4.6: **Intensity dependence of final kinetic energies and photoelectron spectra in very small near-fields (≈ 3 nm).** (a) Linear plot of photoelectron spectra averaged over all the field cycles in the pulse. (b) The final kinetic energy of the electrons at the central field cycle is shown. Arrow 1, shows a shift of the turning point towards higher energies and later emission times, while Arrow 2 indicates an increase in the slope (with respect to the energy axis) of the tangent near the region of constant energy drop of the direct electrons.

feature observed is a shift of the low energy peak on the photoelectron spectrum. It corresponds to a shift in final energy of electrons at the direct-indirect transition region. Here, the electrons experience an increasing near-field gradient which causes this shift in energy. The shift appears to be quite significant at small decay lengths and has not been discussed in any of the related literature. In case of a few-cycle pulse, like the ones used in our experiments, multiple low energy peaks are expected to appear from the other laser field cycles in the pulse. As shown in Figure 4.6 (a), the photoelectron spectra exhibit three such peaks in the low energy region corresponding to the transition point in the final energy plot of each cycle. The difference in energy positions are a result of different field strengths in each cycle. Another observation is made where the maximum energy of the direct (sub-cycle) electrons increases rapidly with intensity. It leads to an increase in the absolute slope in the final energy curve of the direct electrons near the transition (see Figure 4.6 (b)), caused by an increased field strength and hence larger ponderomotive energy. This smears out the electron count distribution on the energy axis broadening its peak width. The broadening is proportional to the intensity, and is independent of the near-field decay length. However, the proportionality factor changes when the decay length is close to the quenched region.

In summary, the low energy peak shift is caused by a change in the near-field gradient. The gradient can be changed either by changing the near-field decay length or the intensity. A variation in intensity, proportionally changes the width of the peak as well. The re-scattered or high energy electrons are strongly affected by decay lengths near the quenched region. Hence, a sign of deviation from the $10U_P$ cutoff law in the photoelectron spectrum strongly indicates quenching effects due to a small decay lengths.

2D averaging

To reproduce more realistic effects of the near-fields, 2D emission profiles from the tips are investigated. For this, the complete 2D electron emission probability distribution is used (see Figure 4.2). The final kinetic energies are calculated for each position on the tip and emission time with respect to the laser field. They are graphically represented in the form of color maps (see Figure 4.7). The kinetic energies shown here are not weighted according to their emission probability, and their observable change with the position is purely due to changing strength and decay length of the near field (see Figure 2.3 (a)). However, the corresponding energy spectrum is computed by taking the emission probability in account. No big difference is observed between the 1D and 2D averaged spectrum for both the tip sizes considerations. The 2D plots appear much smoother due to their higher electron yield. The peak features observed in the spectrum of the 3 nm tip in 1D (see Figure 4.6) are preserved in the 2D averaged spectra. This is expected as the emission probability is much higher near the apex where the near-field is almost constant. Also, the small acceptance angle of the time of flight spectrometer, prevents averaging the kinetic energies of electrons emitted over a

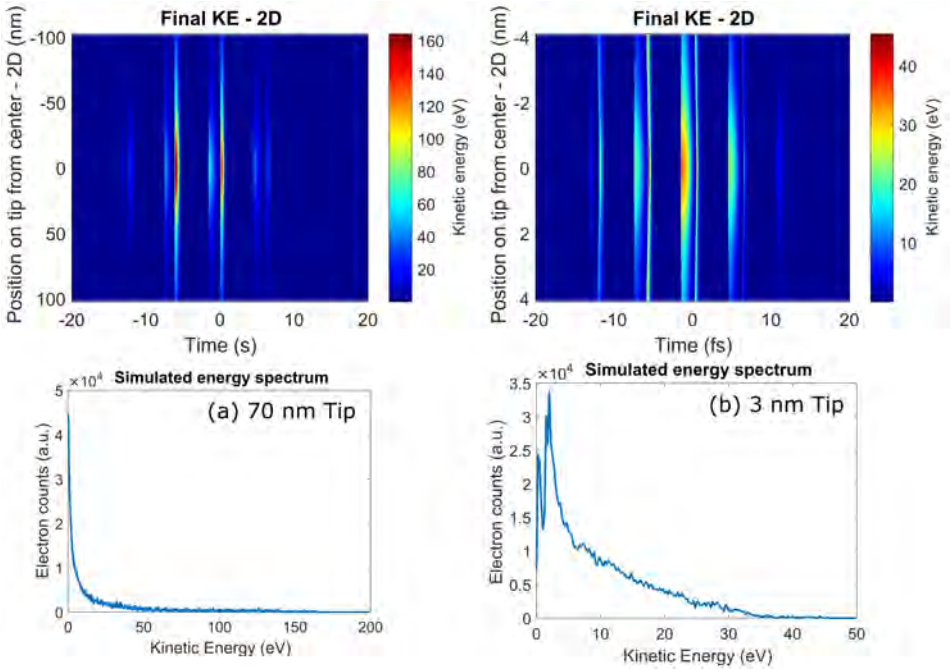

Figure 4.7: **2D - spatially averaged final kinetic energy map and energy spectra.** The data has been shown twice for two different tip dimensions with different field decay lengths. The intensity of the incident pulse for both the cases were kept at 1×10^{12} W/cm^2. The final kinetic energies are displayed as color maps, but essentially represent the same plots as shown in Figure 4.4.

large region. The shape of the spectrum qualitatively fits well with the experimentally obtained spectra.

Chapter 5

Results and discussion

In this chapter, the results obtained from the experiments are illustrated and analyzed. First, the ionization spectra of Argon and Xenon are discussed to obtain an understanding of how the results from the nanotips are calibrated. After this, the results from nanotips are reported and analyzed in two sections. They are categorized under their respective laser wavelengths used. Each section contains a short introduction to some of the experimental methods specific to the measurement, followed by a detailed discussion on the obtained results.

5.1 Gas calibration

After the availability of high power pulsed lasers, gases were best suited for experimental studies in strong-field physics, and have been investigated extensively ever since [14, 47, 22, 17, 48, 36]. Fairly accurate numerical results with single-atom models and ease of experimental implementation make them a benchmark in strong-field physics. Although, the primary aim of this thesis is to investigate such dynamics in metallic nanostructures, experiments are carried out in gas as a reference for optimizing the system before carrying out measurements with tips.

The process of optimization is made possible by a gas nozzle in the experimental chamber as explained previously (see Figure 3.6). The gas nozzle is brought near the laser focus using the translation stages with visual feedback from an in-situ microscopy setup (see Figure 3.7). After this, the gas valve is opened to increase the chamber pressure by approximately 5×10^{-6} mbar. The electron emission from the gas allows optimization of various parameters by observing the count rate, as described henceforth. The gas nozzle is coarsely aligned such that there is maximum overlap between the gas flow and laser focus. However, sufficient nozzle-focus distance is maintained to obtain a relatively uniform distribution of gas density in the focus. Slight misalignment of the beam on the parabolic mirror results in large deviations in focus size and obtained intensity. This is utilized to our benefit by obtaining very precise feedback from fine tuning of the beam alignment onto the mirror. The feedback is obtained in

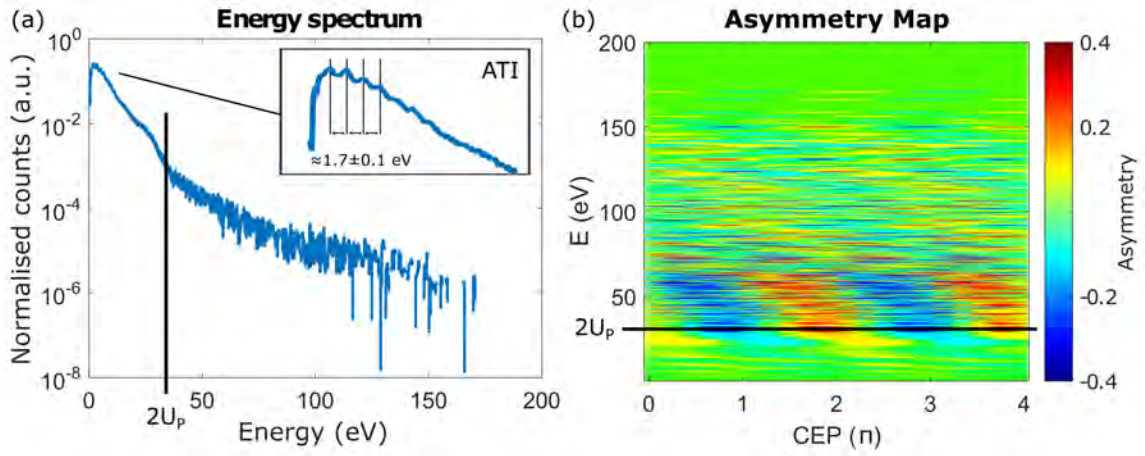

Figure 5.1: **Photoionization spectra of Argon with 5 fs pulses.** (a) CEP averaged energy spectrum. (b) Asymmetry map. ATI indicates above threshold ionization peaks and U_P is the ponderomotive energy. The laser pulse intensity is 3.68×10^{14} W/cm^2 (calculated from $2U_P$).

terms of the emission count-rate obtained from the gas. The angle of polarization is also checked making sure that it is parallel to the TOF entrance axis, which also results in maximum electron counts. The gases used are Argon and Xenon with an ionization potential of 15.76 eV and 12.13 eV respectively. Argon is used with 700 nm laser pulses leading to a lowest multiphoton emission order of 9, and of 17 in case of photoemission from Xenon which is used with 1800 nm pulses. Such high non-linearities make the electron count-rate extremely sensitive to intensity and focal volume modulation's in the laser focus, and is much more sensitive as compared to carrying out these optimizations directly with nanotips. Intensity modulations are also brought about by variations in the pulse duration. This is optimized by compensating for extra chirp in the pulses with a pair of glass wedges. The optimizations are performed chronologically in the mentioned order and prove to be very useful in regulating optimal beam conditions before carrying out measurements with tips.

5.1.1 Argon Spectra

Argon is used to obtain CEP resolved reference spectra for the tip measurements with 700 nm, 5 fs pulses. The energy spectrum obtained consists of a low energy region which includes the electrons emitted by tunneling (direct electrons). The electrons are then accelerated by the laser field without undergoing any scattering, and reaching maximum energies up to $2U_P$. This region is also populated by electrons emitted by multiphoton ionization processes including above threshold ionization [49]. A close-up on the low energy part (see Figure 5.1(a)) reveals the above threshold ionization peaks in the spectrum. The lack of sharpness of the peaks are a result of the broad range of

photon energies present in the pulses we use. The energy spectrum also includes electrons with energies beyond the $2U_P$ mark and comprise of electrons (indirect electrons) which undergo elastic scattering. They are produced by light induced tunneling, and are accelerated back by the laser field to undergo elastic scattering (see Section 2.3.2) with its parent atom. This results in electron emission with broad range of energies with constant yield, before sharply cutting off at energies around $10U_P$ [47]. This is commonly referred to as the re-scattering plateau. In the illustrated measurement (see Figure 5.1) the $10U_P$ cutoff is not clearly distinguishable because of poor statistics, but the $2U_P$ region is fairly distinguishable. The asymmetry map comes of help here (see Equation 3.4) where the CEP dependent modulation of the spectrum is clearly highlighted. The direct electrons do not show strong CEP dependence as the tunneled electrons are overlapped with different emission mechanisms like multiphoton emission, which are not affected by the CEP as discussed earlier. They may also include electrons which tunnel from the intermediate states below the Coulomb barrier. The re-scattered electrons, however, exhibit strong CEP dependence as higher energies are primarily reached by the scattering process due to its back acceleration in sub cycle fields. Also, the multiphoton electron counts drop exponentially with increasing energies due to the higher order emission process which decreases the ionization rate at high energies. Thus, a clear distinction between the two regions is obtained. This distinction in the asymmetry spectrum corresponds to a kink where the re-scattering plateau evolves. The determination of U_P by this method gives us an estimate of the intensity (see Equation 2.10). As the measured average-power scales linearly with intensity, we use this estimate to calibrate the power-intensity conversion for the spectra obtained from nanotips.

Also, intensity varying scans were carried out with the long pulses (25 fs) taken directly from the amplifier. These pulses have much narrower spectral bandwidth in contrast to the broadband 5 fs pulses. Thus, they form sharp above-threshold ionization peaks (see Figure 5.2). The peak-spacing obtained is 1.66 ± 0.03 eV, which is very close to the center photon energy of the long pulse (1.64 eV$\leftrightarrow$756 nm), verifying the energy calibration of the system.

5.1.2 Xenon Spectra

The peak intensities achievable with the 1800 nm laser pulses were not enough to generate sufficient electron counts to observe the Argon spectrum. However, Xenon with its lower ionization potential turned out to be a suitable alternative. The spectrum has been recorded with 18 fs pulses and the procedure was kept same as described for Argon. Another consequence of the limited pulse energy was that an in-situ CEP control and tagging could not be implemented. Thus, for calibrating the intensity of measurements on the nanotips carried out with this laser, we used the position of a kink where the re-scattering plateau begins in the Xenon spectra, to determine $2U_P$ (see Figure 5.3). The Xenon spectra also exhibits above-threshold ionization features with

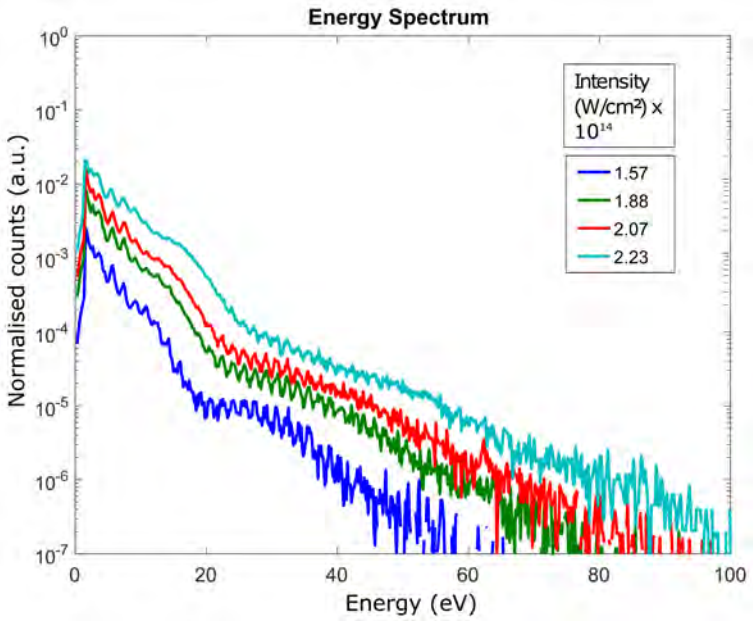

Figure 5.2: **Photoionization spectra of Argon with 25 fs pulses.**

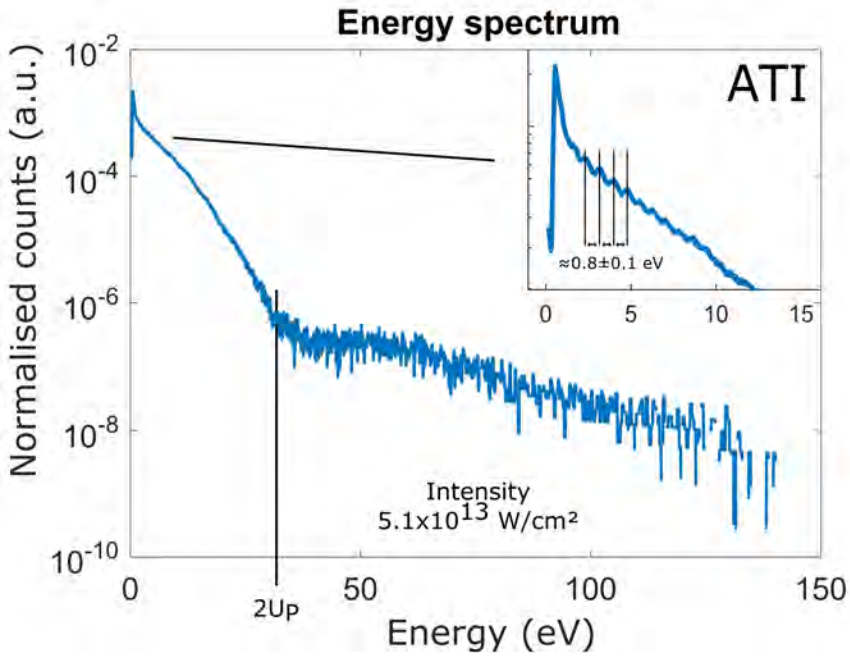

Figure 5.3: **Photoionization spectrum of Xenon.** ATI are the observed above threshold ionization peaks.

a peak spacing of 0.77±0.07 eV, where the center wavelength of the laser corresponds to 1800 nm ↔ 0.69 eV.

5.2 Measurements with nanotips

After the laser pulses at the focus of the parabolic mirror have been characterized, the linear motorized stages are used to position the nanotips in the focus. The same two-step procedure of coarse alignment is carried out, using visual feedback from the in-situ microscope setup, followed by fine alignment observing the electron counts. In case of tips, the process is a bit more challenging given the dimensions of the apex and high probability of misleading counts generated from other surfaces of the tip. As a secondary check, in case of 700 nm pulses, one can observe a distinct image on Channel 1 (see Figure 3.6), formed by scattering of the laser pulse. However, this does not work in case of 1800 nm pulses as there is no linear response on the image sensor at this wavelength, and the back scatter is not strong enough to generate a non-linear response.

5.2.1 Emission at 700 nm

Gold nanotips are irradiated with broadband laser pulses at a center wavelength of 700 nm with pulse durations of 5 fs. The photoelectron spectrum is recorded by varying the intensity of the laser pulses (see Figure 5.4) over the complete dynamic range of our setup. Part of the motivation for this experiment has been to explore multi-electron effects, and keeping that in mind, the dynamic range was kept at 100 - 20000 electron counts recorded per second. The range was chosen to obtain reasonable statistics on the lower side, and to prevent laser induced damage to the gold nanotip on the higher side. Given the repetition rate of the laser, detection efficiency of the MCP and collection angle of the TOF, we estimate 1 to 200 electrons being emitted per pulse, distributed across the complete intensity range. Every measurement for a particular intensity was integrated over a time span of 200 s. The spectra are labeled with their respective incident intensities while the intensities actually experienced at the apex are much higher due to field enhancement [50]. The field-enhancement factor $E_0(r)$, is a ratio between the applied and obtained electric fields as a function of the position on the tip (see Figure 2.3). Hence, the resultant intensity increases by a factor of $E_0(r)^2$.

The first observable feature of the spectrum is the appearance of a broad low energy peak. This is often a signature of multi photon emission and consequently the weak-field regime. The work function of polycrystalline gold was taken as $\phi = 5.1$ eV [51]. Thus, an electron would require 2.88 ($\approx$3 to satisfy the lowest integer order) photons to overcome the Coulomb barrier as shown in Figure 2.4 (a). A common check to judge the photoemission regime is to see how the emission current (count) scales with the incident intensity. The same is done for the obtained spectra (see Figure 5.5 (a)), where

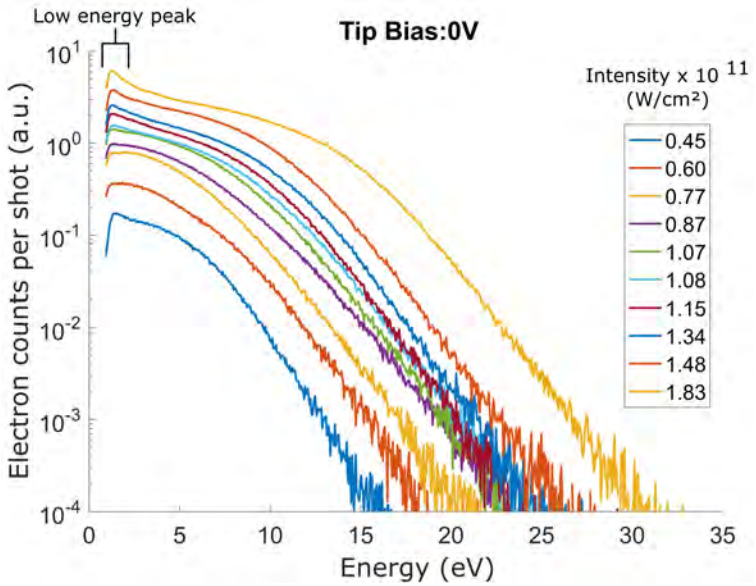

Figure 5.4: **CEP averaged photoelectron energy spectra of the gold nanotip.** Laser pulses at 700 nm were used and the intensity was varied to obtain the spectra.

the scaling of the emission integrated over all the energies, and at an energy where the low energy peak is prominent, are plotted. As a reference, we have also included the ideal scaling plots for a 3rd order multiphoton and linear emission rate scaling. The figure depicts the counts at the peak to be scaling very close to an order of 3 ($\propto I^3$) indicating emission in the multiphoton regime. The total counts scale very close to this slope as well, hinting at the majority of the electrons undergoing a three photon emission process.

The second noticeable feature of the energy spectrum is the plateau-like feature that appears right after the low-energy peak. In case of pure multiphoton emission at higher energies i.e. ATI effects, the count rate should drop exponentially with every order following the multiphoton scaling. The contrary indicates strong-field effects. A common signature of strong-field emission is the re-scattering of tunneled electrons, depending on their birth times with respect to the phase of the laser field (see Section 2.3.2). This process is highly sensitive to sub-cycle changes in electric field strength of the laser pulses. Hence, the final (terminal) kinetic energy of the electrons can be resolved by varying the CEP, as shown before in case of atoms with argon (see Section 5.1.1). This has been shown in the asymmetry maps for the spectra obtained at certain intensities in Figure 5.6. As expected, CEP dependence is weak at lower energies as the multiphoton processes which dominate, are not sensitive to the sub-cycle electric field modulation. However, we observe larger asymmetries (CEP dependence) towards the high-energy side of each spectrum. The asymmetry plots also show that the energies at which there is strong modulation in CEP, shift with the intensity, as expected. In case of re-scattered electrons, the electron's energy-gain is proportional to

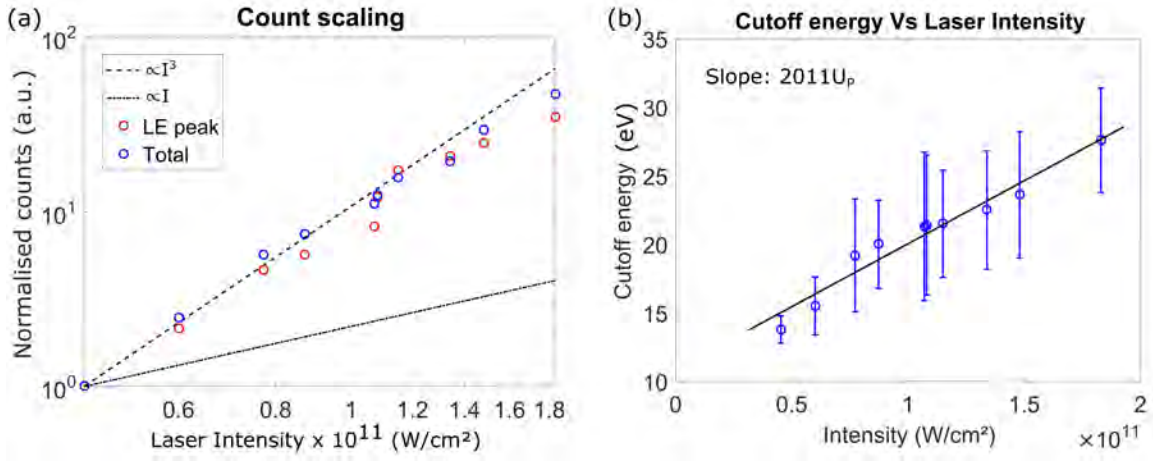

Figure 5.5: **(a) Scaling of electron counts with incident laser intensity.** The figure shows how the electron counts scale with incident intensity at the low energy peak (LE peak) and the total counts. The lines in black are used as a reference to indicate the third and first order exponential scaling with intensity of the laser. **(b) Plot of estimated cutoff energy against laser intensity.** The linear fit from the scaling plot is used to determine the slope in terms of U_P, and also to re-calculate the respective cutoff energies for each incident intensity. The slope obtained ($slope_{OB}$), is used to estimate the electric field enhancement factor, which turns out to be about 14 (see Equation 5.1). The enhancement factor is also used to estimate the real (enhanced) intensities at the tip apex, which in-turn, gives an estimate of the emission regime. This is inferred from the Keldysh parameters (γ) for the respective enhanced intensities (see Equation 2.9) and are found to be [1.3, 1.24, 1.19, 1.16, 1.11, 1.1, 1.09, 1.05, 1.02, 0.96]. This is explained further in the text.

the ponderomotive energy U_P, which in-turn scales linearly with the laser intensity (see Equation 2.10). This has been confirmed in case of metal nanotips in the single-electron emission regime [23].

The cutoff energies for the shown spectra, are estimated from the asymmetry map where the modulation reduces below 0.2 towards the higher energy side (see Figure 5.6). These values are shown in a plot against the laser intensity (see Figure 5.5 (b)). The slope obtained from the linear fit of this plot gives the scaling factor. In case of atoms (gases), the cutoff energy scales with a slope of $10U_P$ (see Equation 2.13). However, in case of nanostructures, the scaling factor is higher, due to added contributions from field-enhancement (see Section 2.2). The deviation in slope from $10U_P$, is used to determine the field-enhancement factor ξ, given by the relation

$$\xi = \sqrt{\frac{slope_{OB}}{10U_P}}\,, \tag{5.1}$$

where $slope_{OB}$ is determined from the measured scaling plot (see Figure 5.5 (b)) in terms of U_P. The effective intensity at the tip apex can be determined from the known incident intensity, as it is amplified by a factor of ξ^2. To obtain a quantitative estimate of the emission regime, the Keldysh parameters are determined using Equation 2.9 and Equation 2.10, by replacing I_L with the effective intensity. The obtained values are shown in Figure 5.5, which indicates that the emission takes place in a mixed regime. This correlates well with the indications from the experimental data. However, the deviation in slope (with respect to $10U_P$) may also occur due to space charge[1] effects. Space charges are formed when too many electrons are emitted by the laser pulse at timescales comparable to the laser pulse duration. It results in Coulomb interactions between the electrons themselves. One observable effect of that is the added acceleration of the re-scattered electrons towards the detector by repelling Coulomb forces from an electron cloud formed near the tip apex. This has been observed and discussed in recent works on nanotips [29] and dielectric nanospheres [52, 53]. The large field-enhancement factor obtained, along with the emission of up to 200 electrons per pulse, hints at added acceleration of the re-scattered electrons due to space charges.

In general, electron emission from the nanotips are measured while they are grounded, i.e. at an equal potential with its surroundings. However, one set of measurements were carried out by applying a small bias voltage of $-30V$ on the tip. The spectra obtained are shown in Figure 5.7 (a). The applied potential, leads to a few noticeable changes in comparison with the spectra measured without any bias (see Figure 5.4). One is the broadening of low energy peaks and the other is suppression of the re-scattered electrons. Some preliminary 1D quasiclassical simulations of the three step model, with an assumed exponential field-decay length of 5 nm, and small bias voltages, reveal similar effects (see Figure 5.7 (b)). From the simulation, the effect of the bias voltage can be understood as a constant shift about the zero-magnitude of the effective

[1] Continuum of electrons distributed over a region of space

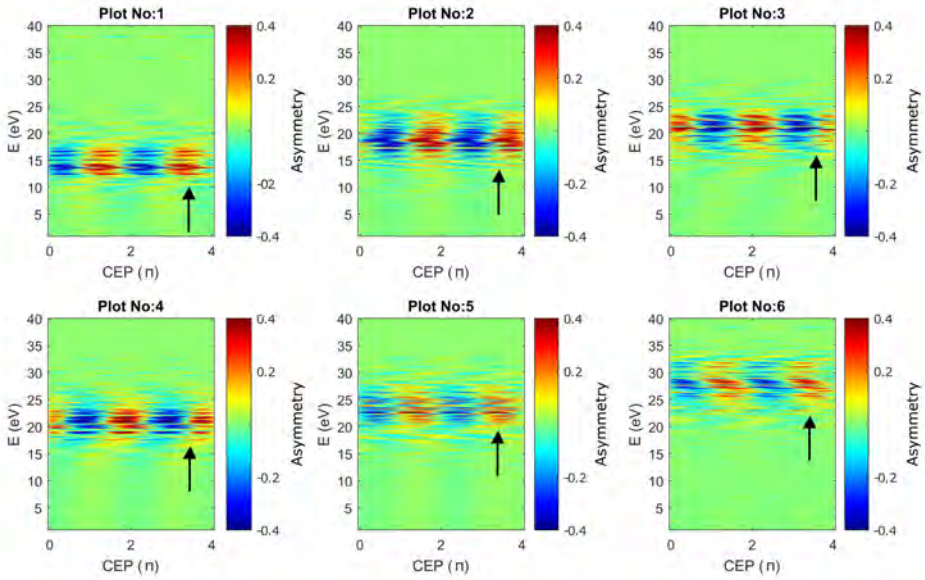

Figure 5.6: **Asymmetry maps at different intensities.** The incident laser intensities of the corresponding plots [1-6] are $[0.45, 0.77, 1.07, 1.15, 1.48, 1.83] \times 10^{11}$ W/cm^2. The arrows show the shift of the strong modulation region towards higher energies with increasing intensities.

oscillating electric field strength. This leads to an asymmetry between the front and back accelerating fields, resulting in reduced probability of electron re-scattering.

5.2.2 Emission at 1800 nm

After carrying out the measurements with 700 nm laser pulses, the experimental chamber was relocated and used with a different laser setup. Here, similar gold nanotips were irradiated with broadband laser pulses at a much larger center wavelength of 1800 nm and pulse duration of 18 fs. It was not possible to control and tag the CEP of the pulses owing to the low pulse energies that were available. The pulses were delivered at a rate of 100 kHz, allowing decent statistics even at very low count rates. In this case, the dynamic range was kept at approximately 100 to 50000 electron counts per second over the whole intensity scan. This translates to the emission of 0.1 (statistically) to 50 electrons per pulse. According to theory, a scaling of the wavelength towards mid-infrared, strongly affects the Keldysh parameter and pushes the emission regime deeper into tunneling. The ponderomotive energy gained by the electrons scales with the square of the wavelength (see Eqn 2.10), which lowers the Keldysh parameter (see Equation 2.9) significantly. This can also be intuitively understood by considering the electric field oscillations in the pulse. For longer wavelengths, the potential barrier is suppressed for a longer duration, leading to a more DC-like behavior and making it easier for the electrons to undergo tunneling.

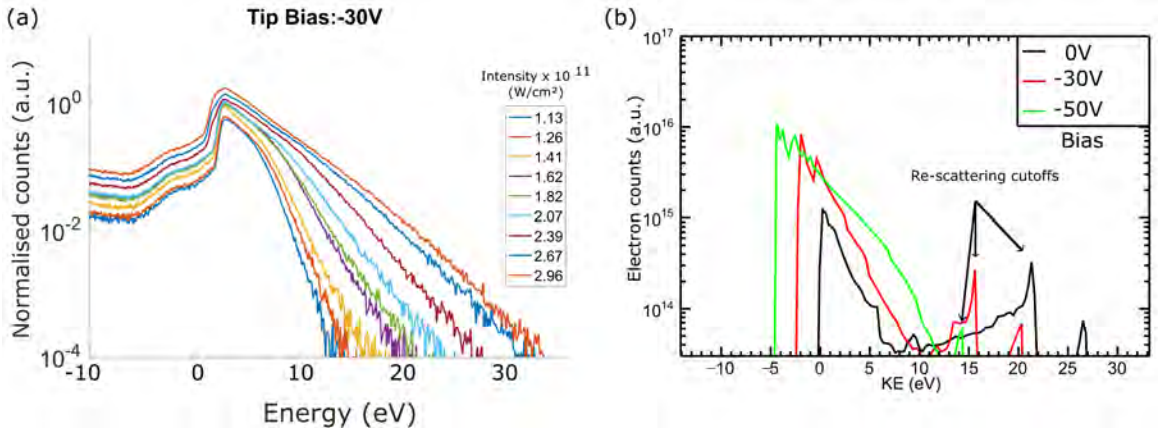

Figure 5.7: **Photoelectron spectra of a biased tip.** (a) CEP averaged spectrum from the experiment. The energy axis has been subtracted by the energy gained by the electrons in the DC field. (b) Simulated energy spectrum with a varying bias voltage. This simulation was performed at an effective intensity of $5 \times 10^{13}\,\mathrm{W/cm^2}$ with a decay length of 5 nm (courtesy of J. Schötz).

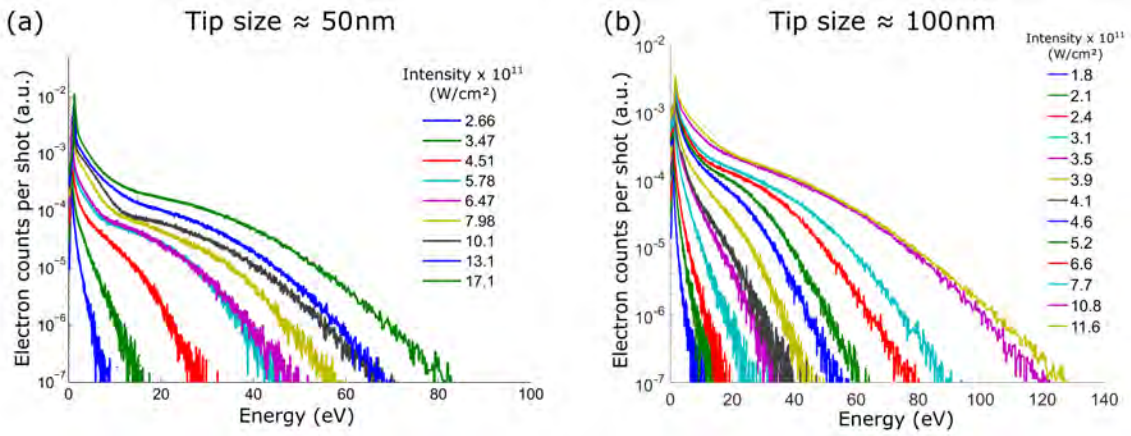

Figure 5.8: **Energy spectrum of electrons emitted by 1800 nm laser pulses at gold tips with different tip radii.** The intensities labeled are the incident laser intensities. The real intensities as experienced by the electrons are higher depending on the field enhancement at the tip apex.

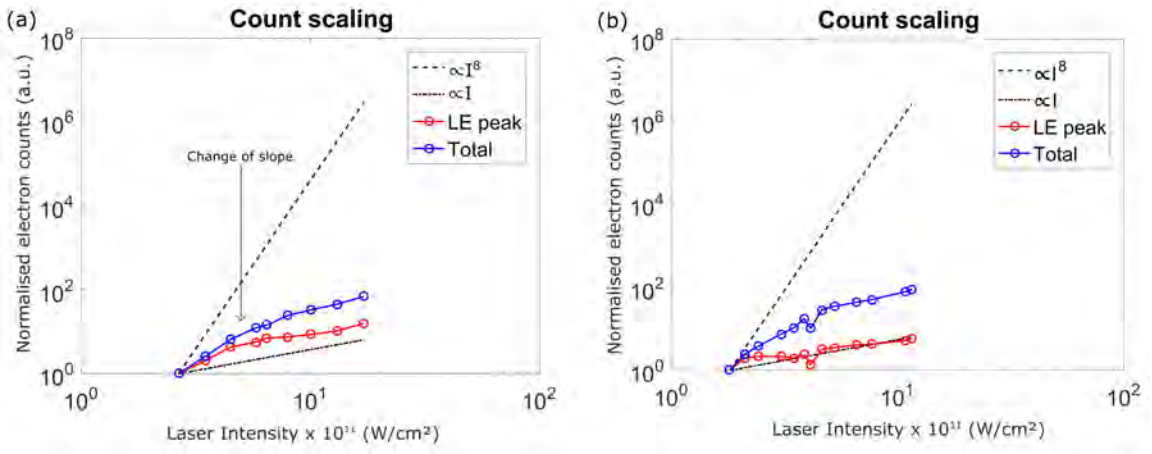

Figure 5.9: **Scaling of electron counts with laser intensity for 1800 nm pulses.** (a) 50 nm Tip, (b) 100 nm Tip. The electron counts obtained at the low energy peak (LE peak) in Figure 5.8 in blue, and the total counts in red have been plotted against their respective laser intensities. The exponential scaling fits of order 8 and 1 are plotted in black as a reference.

Similar measurements were carried out for 1800 nm pulses (see Figure 5.8) on two different gold nanotips. Here, a very sharp low-energy peak is observed with the onset of a plateau-like feature after it. The difference in counts between the low-energy peak and plateau is more than an order of magnitude, contrary to the case when irradiated with 700 nm, hinting at a different emission mechanism. The tip radii were determined by SEM imaging after the experiment. Even though this estimation might not be very accurate, it was enough to judge that the tip shown in Figure 5.8 (a) was considerable smaller than the one in Figure 5.8 (b). The spectrum, however, shows contradictory results to what is ideally expected in such a scenario. In general, tips with smaller radii lead to higher field enhancement (see Section 2.2), resulting in higher energy of the direct and indirect electrons. Such contrary behavior indicates that the emission could be from a much sharper localized nanostructure on the tip surface. It would be interesting to verify this point by implementing field ion microscopy (FIM) or field emission microscopy (FEM) techniques.

A scaling plot of counts of the low energy peak and the total counts (see Figure 5.9) reveal that the emission deviates strongly from its multiphoton scaling, indicating tunneling. The dominant photon energy corresponds to 1800 nm (0.69 eV) and requires 7.4 ($\approx$8 to satisfy the lowest integer order) photons or more to be emitted by multiphoton effects. A close correlation between the scaling of total counts and peak counts indicate the dominance of emission by tunneling. For the 50 nm tip, it is also observed that the count scaling slope gradually changes with higher intensity, starting from somewhere between 8 and 1, and ending up below 1. The change of slope can be explained in terms of the increase of U_P resulting in further decrease of γ, moving deeper into tunneling

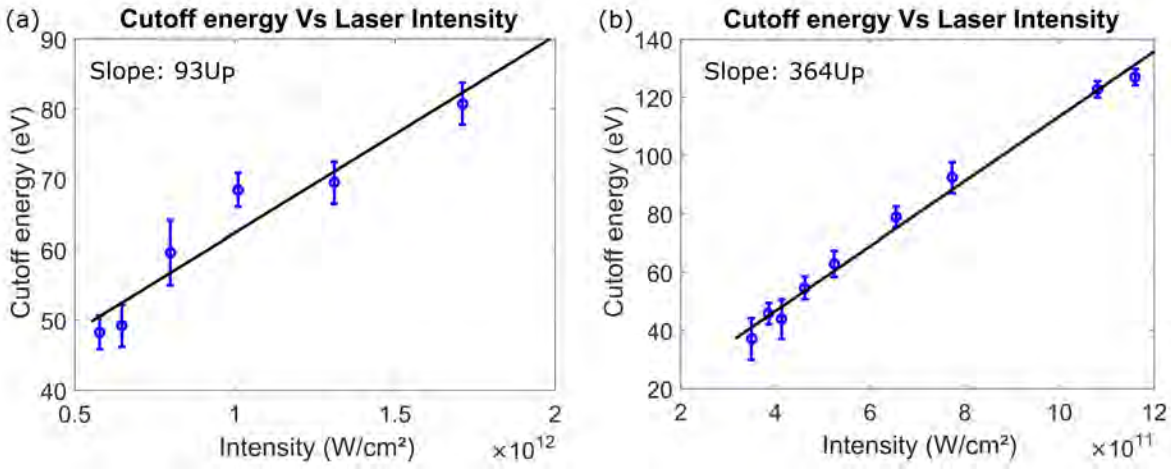

Figure 5.10: **Plot of estimated cutoff energy against laser intensity.** (a) 50 nm Tip, (b) 100 nm Tip. An approximate cutoff energy is estimated from where the plateau sharply falls off in Figure 5.8. The intensities, for which the spectra show clear evolution of a plateau, are the only ones which have been considered for the plot.

regime. This transition has been observed from tungsten tips at smaller wavelength's [50]. Also, around an intensity of 5×10^{11} W/cm^2, the spectrum starts to develop a plateau-like feature (see Figure 5.8). Normally, re-scattered electrons are responsible for this plateau-like spread in energy and an increased visibility of tunneled electrons could explain the sudden prominence of the plateau around this intensity. The 100 nm tip exhibits a lower slope from the beginning at similar intensities. This is possibly due to a higher field enhancement, assuming the presence of localized peaks. This assumption is also supported by the observation of higher energy electrons from the 100 nm tip as compared to the 50 nm tip, at comparable intensities. The, sudden appearance of a plateau is not observed in the emission spectra for the 100 nm tip. This is also supported by the scaling plot where it appears to be constantly in the tunneling region. The strong indications of tunneling emission in the low energy region is not so commonly reported in literature.

For these measurements, CEP resolved data was not available and it could not be verified if the cutoff region consists of re-scattered electrons. In-case of re-scattered electrons following the cutoff law (see Equation 2.13), the maximum energy gained, scales linearly with intensity. The maximum energy is determined from the spectrum where the counts appear to sharply drop after the plateau. Figure 5.10 (a) does not convincingly show a linear behavior, but (b) of the same figure gives a better indication of linear scaling at lower intensities. However, if the emission is from a localized smaller nanostructure, as assumed, the enhanced fields have a much smaller decay length. This leads to a departure from the ponderomotive linear scaling [26]. In general, this occurs if the wavelength is very large or the decay length of the enhanced field at tip apex is very small. For very small decay lengths, the electron can escape the laser field

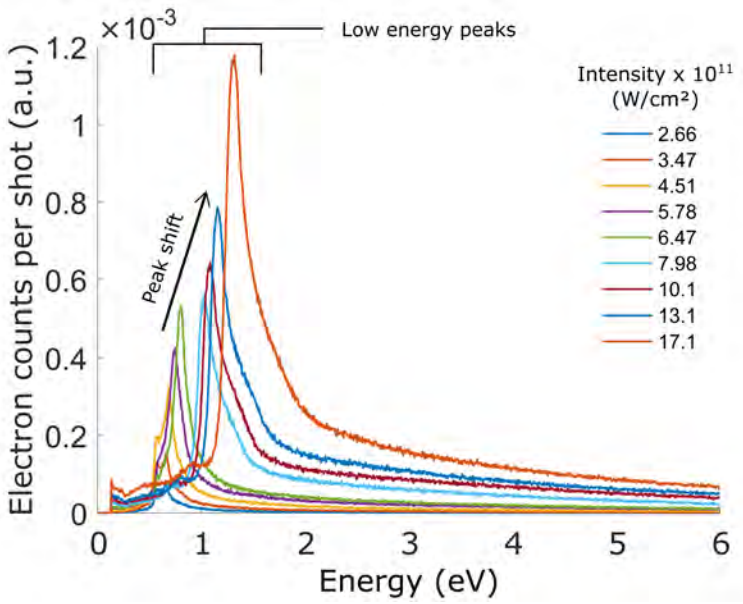

Figure 5.11: **Low energy peaks of emission spectra with 1800 nm laser pulses.** The spectra have been plotted on a linear scale on the Y-axis to enhance the visibility of the low energy peak. Both the peak position and peak width increase with an increase in intensity.

before the pulse finishes. To estimate the limiting decay length, the dimensionless adiabaticity parameter δ is used (see Section 2.3.2) for the given configuration. The emission is expected to be within the quiver regime (linear scaling region) for field decay length's $(1/e)$ down to about 5 nm. In case of emission from the complete tip, we expect the decay length to be comparable to the tip radius according to our simulation model (see Section 4.1). The linear scaling would still remain valid, resulting in Keldysh parameters for the measurements to be in the range of 1 to 0.4. These values have been calculated from the slope of the linear fit in Figure 5.10 (b), following the same procedure as described in Section 5.2.1. The electric field enhancement factor is determined to be around 6 (calculated using Equation 5.1). Similar calculations from Figure 5.10 have been omitted due to its large error bars. The estimate of the Keldysh parameters, clearly indicate the emission to be closer to the tunneling regime as compared to the emission with 700 nm pulses.

A particularly interesting feature of the spectra obtained from these measurements are the prominent low energy peaks. Figure 5.11 shows these peaks prominently on a linear scale. Peaks as narrow as 0.2 eV (FWHM) could be obtained in the energy domain. Very similar spectra with a sharp low-energy peak has been predicted from 2D quasiclassical calculations [42], but have not been observed experimentally. One possible reason for the broadening of the low energy region shown in [42] could be due to a large percentage of electrons appearing from other mechanisms like multiphoton and photo-field emission [54]. The spectral characteristics of these emissions are quite

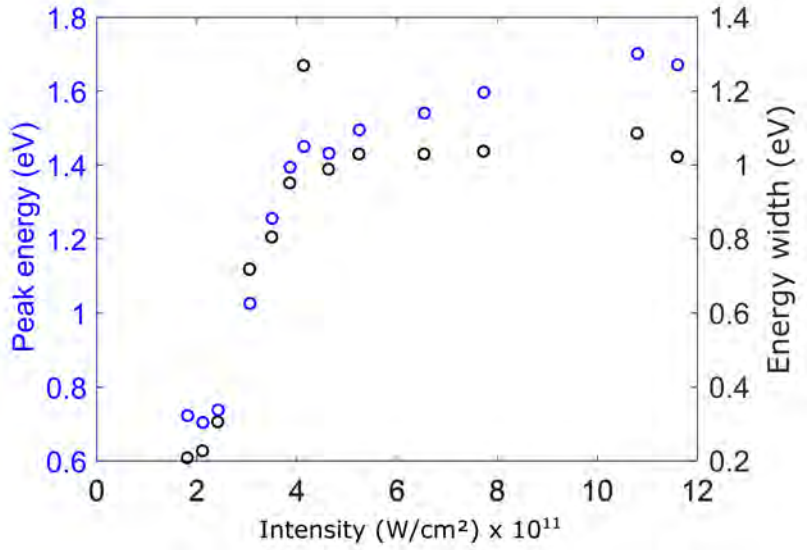

Figure 5.12: **Scaling of low energy peak position and energy width, with intensity.** The data points in blue represent the energies at which the low energy part of the spectrum peak's for their respective intensities while the black data points represent the energy bandwidth (FWHM) of the same.

sensitive to electron-electron and electron-phonon scattering effects in metals and may lead to broadening [7]. These emission processes dominate when the photon energy gets closer to the work function of the material i.e when the non-linearity in count scaling is reduced. The 1800 nm laser pulses used in our case, increases this non-linearity and thereby possibly suppressing the multiphoton and photo-field emission processes to a large extent. This is also supported by the obtained count scaling (see Figure 5.9) which indicates dominance of tunneling especially at the low energy peaks. The scaling does not distinctly rule out the possibility of photo-field emission as it scales quite close to $\propto I$. It also makes sense given the data obtained with 700 nm laser pulses, where the low energy peak scales quite close to its multi-photon order with a broad low energy peak.

The low energy peaks also shift in the peak-energy positions and peak width (FWHM) with varying intensities. This is quantitatively shown in Figure 5.12. Simulations (see Figure 4.6) indicate similar effects when varying the intensity. As established in Chapter 4, increasing the intensity, increases the electric field gradient of the near-field at the tip apex. The increased gradient is responsible for shifting the peak position to higher energies, and increasing the peak width as well (see Section 4.2). This effect is independent of the quenching effect and should occur irrespective of the tip size. However, as this explanation holds true in case of strong-field emission from the simulations, it stands out as another indirect indicator of electron emission by tunneling.

In the referred simulations in Section 4.2, considering a large tip of about 70 nm

(close to the tip size estimated by SEM imaging), the experimentally observed low-energy peaks could not be reporoduced. The low-energy peak obtained in the simulation (see Figure 4.4) remained close to zero energy. As the peak shift depends on the near-field gradient, a desired shift could be produced in the simulation by increasing the intensity. However, this also results in electrons re-scattering with very high final energies (see Equation 2.13), much higher than what is experimentally observed. The other way to increase the electric field gradient would be to reduce the decay length of the near-field. The advantage of this modification is that, although a peak shift is produced, the energy gained by re-scattered electrons can be suppressed due to electrons escaping the small near-field region before the laser pulse is over (outside the quiver regime). Hence, a set of simulations were carried out assuming emission from a smaller tip (resulting in a small near-field decay length), representing a localized emission site, as also predicted in the beginning of this section. In this simulation, the tip size was chosen such that its near-field decay length was about 3 nm, which is beyond the quiver limit and the electron experiences quenched motion. These simulations in 1D could reproduce a similar low energy peak (see Figure 4.6). The simulation spectra contains three split peaks in the low-energy region. Each peak arises from electrons emitted within a negative electric field cycle of the laser pulse (see Figure 4.4 (a)). The difference in the electric field strength of each field cycle in the pulse, produces a different near-field gradient, resulting in peaks at different energy positions on the energy spectrum.

To obtain a more quantitative correlation between theory and experiment, the same simulations were carried out in 2D (see Figure 4.7). The 2D simulated spectrum was then matched with an experimentally obtained spectrum (see Figure 5.13). This was done by adjusting the simulation intensity to match the peak-shift and the high energy tail at the same time, for a specific experimentally obtained spectrum. The chosen tip structure, with a decay length of 3 nm, produced a close correlation with the experiment. The low energy peak structure, along with the high energy tail appear well correlated. The relatively good correlation supports the simulation model and its proposals.

In the spectrum obtained from the experiment, we observe one large low-energy peak, preceded by a smaller secondary peak structure on the energy axis. This is explained in terms of emission from different field-cycles of the laser pulse, combined with a spatial average over the tip apex. It appears that the 2D averaging (see Figure 4.7 (a)) smoothens out the discrete low-energy peak separation obtained in the 1D simulation (see Figure 4.6 (a)). Two of the three peaks obtained from the 1D simulation tend to merge, leading to a similar feature as obtained in the experiment. The smoothening takes place possibly due to a varying field gradient over the surface of the tip apex (due to a position dependent field enhancement factor), causing slightly different peak shifts at each position on the tip. Hence, the near-field gradient appears to be the most important parameter that governs the characteristics of the low energy peaks. As the splitting of the low-energy peaks appear to be dependent on the number of cycles in a

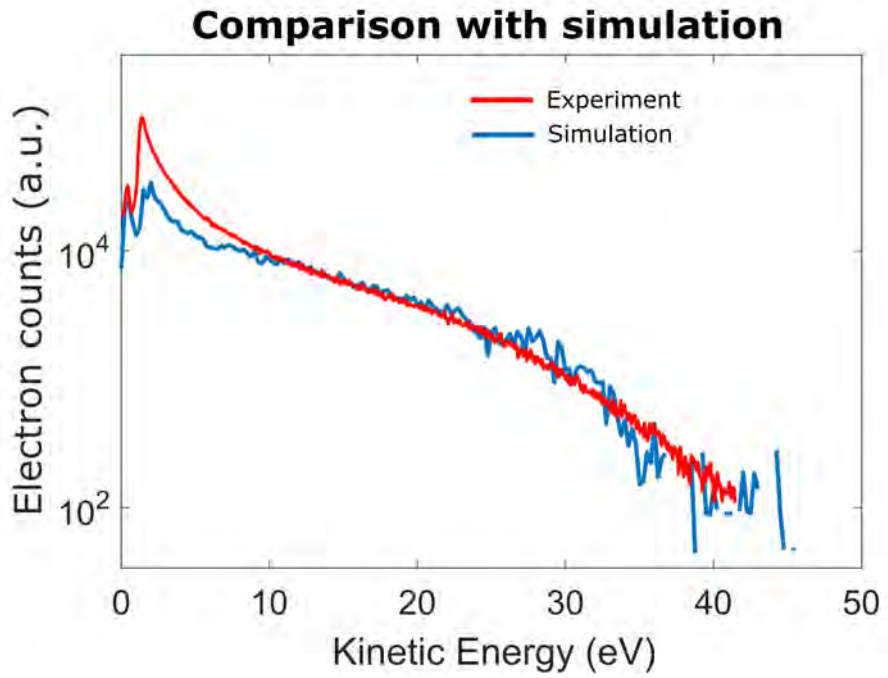

Figure 5.13: **Comparison of experimentally measured and simulated electron energy spectrum.** The incident laser intensity for the experimental spectrum is 4.6×10^{11} W/cm^2. The effective intensity of the laser at the tip apex in the simulation is 6.9×10^{13} W/cm^2. The effective enhancement in this case is about 12. It is calculated using the relation $\xi = \sqrt{I_{inc}/I_{eff}}$, where I_{inc} is the experimentally obtained incident intensity and I_{eff} is the effective intensity from the solution.

laser pulse, it should be possible to do away with the splitting by using shorter laser pulses.

The correlation of the high energy electrons, is produced only by assuming a very small decay length in the simulation. Hence, it confirms that the emission experiences quenching as described before. As a consequence, it also supports the idea of electron emission from localized regions on the order of 3 nm.

In the end, the good correlation between experiment and simulation (based on the quasiclassical three step model), stands as another proof of operating in the strong-field regime. In this regime, the observed high-energy features (quenching of the electrons) have been studied and reported [26]. However, the proposed ideas on the low-energy features should contribute to extend our understanding of strong-field photoemission dynamics from metallic nanostructures.

Chapter 6

Conclusion and outlook

The work carried out in this thesis, investigated laser induced photoemission from polycrystalline gold nanotips. Few-cycle pulses were used, centered at wavelengths of 700 nm and 1800 nm. Among these investigations, the work could obtain certain features in the spectra (with 1800 nm pulses) that have not been reported previously. Suitable numerical calculations were performed to elucidate its possible cause.

In the experiments carried out with 700 nm laser pulses, the electrons emitted were found to be dominated by multiphoton emission (weak-field regime). This was primarily concluded from the scaling of electron counts with laser intensity, and faint modulation with CEP variation in the asymmetry maps at the low energies. However, some signs of strong-field emission were obtained in the high energy region of the spectrum, caused due to energy gained by re-scattering of electrons. As seen from the asymmetry maps, the high energy cutoffs exhibit linear scaling with intensity. Using the slope of the scaling, the enhancement factor of the gold tip used was found to be around 14, which is slightly higher than theoretically predicted values [11]. This could be due to space charge interactions leading to a higher scaling slope. The Keldysh parameters obtained for the respective intensities are around 1, hence supporting the idea that the measurements have been recorded in a weak-strong mixed regime.

The 1800 nm laser pulses were used to obtain emission deeper in the tunneling (strong-field) regime. This was confirmed in two ways. First, the slope of electron count scaling with the intensity was found to be far below its multiphoton scaling slope, indicating emission by tunneling. Secondly, the Keldysh parameters were estimated down to 0.4. However, as mentioned before, a highlight of this work was the observation of a narrow bandwidth ($\approx 0.2\,\mathrm{eV}$) low-energy peak. This feature has not been obtained experimentally or explained in any of the previous works on strong-field emission from metal nanotips [55, 42]. A numerical model similar to the one used in [42] was implemented to simulate electron emission from 1800 nm pulses, based on a quasistatic three step model. The low energy peak feature was reproduced by this model, and the observed shift in peak position and width was explained by a change in the near-field gradient with laser intensity. The appearance of multiple peaks was explained and shown to be originating from different cycles of the laser pulse. How-

ever, assuming the experimentally used tip size, the simulation could not reproduce the correct energies for the re-scattered electrons in the measured spectrum. To account for this, the simulation was modified with a small ($\approx 3\,\mathrm{nm}$) near-field decay length to reproduce quenching effects as reported in [26]. With this approach, a decent correlation was obtained between an experimental and simulated spectrum (see Figure 5.13). This assumption supports the idea of a localized emission region on an otherwise large tip, along with a much smaller decay length.

The results obtained are promising, keeping in mind the possible applications. Tunneled electrons could in principle be controlled at sub-femtosecond timescales. Along with this, the yield of electrons in the sharp low energy region is more than an order of magnitude higher as compared to its high energy counterpart. This could be ideal for time resolved applications requiring narrow bandwidth electron pulses for aberration free beam shaping in electron optics.

The findings of this thesis provide a direction for future work, to provide more substantial confirmation of the proposed effects. Further measurements with tip-surface imaging methods like FIM and FEM are proposed. Better estimation of the emission sites are necessary for accurate correlation of experiment and theory. CEP resolved measurements are also desirable as an absolute check for strong-field effects. However, in reality, applications of electron pulses also require good beam intensity i.e. many electrons emitted per pulse. In such cases, electron-electron Coulomb forces come into play altering the energy spectrum. Although we do not see signs of this in our data, it would be interesting to repeat the experiment at higher intensities to emit larger numbers of electrons per pulse.

Bibliography

[1] Ferenc Krausz and Misha Ivanov. Attosecond physics. *Reviews of Modern Physics*, 81(1):163–234, 2009.

[2] Ahmed H Zwail. Femtochemistry:Atomic-Scale Dynamics of the Chemical Bond. *The Journal of Physical Chemistry A*, 104(24):5660–5694, 2000.

[3] P. B. Corkum and Ferenc Krausz. Attosecond science. *Nature Physics*, 3(6):381–387, 2007.

[4] Wayne E. King, Geoffrey H. Campbell, Alan Frank, et al. Ultrafast electron microscopy in materials science, biology, and chemistry. *Journal of Applied Physics*, 97(11):111101, 2005.

[5] H Ihee, V A Lobastov, U M Gomez, et al. Direct imaging of transient molecular structures with ultrafast diffraction. *Science (New York, N.Y.)*, 291(5503):458–62, 2001.

[6] Peter Hommelhoff, Yvan Sortais, Anoush Aghajani-Talesh, and Mark A. Kasevich. Field emission tip as a nanometer source of free electron femtosecond pulses. *Physical Review Letters*, 96(7):1–4, 2006.

[7] Hirofumi Yanagisawa, Matthias Hengsberger, Dominik Leuenberger, et al. Energy distribution curves of ultrafast laser-induced field emission and their implications for electron dynamics. *Physical Review Letters*, 107(8):1–5, 2011.

[8] Fabian Lücking. Carrier-Envelope Phase Control for the Advancement of Attosecond Pulse Generation. *LMU PhD Thesis*, 2014.

[9] F.W. Helbing, Günter Steinmeyer, and Ursula Keller. Carrier-envelope offset phase-locking with attosecond timing jitter. *IEEE Journal of Selected Topics in Quantum Electronics*, 9(4):1030–1040, 2003.

[10] H.R. Telle, G. Steinmeyer, A.E. Dunlop, et al. Carrier-envelope offset phase control: A novel concept for absolute optical frequency measurement and ultrashort pulse generation. *Applied Physics B*, 69(4):327–332, 1999.

[11] Sebastian Thomas, Georg Wachter, Christoph Lemell, Joachim Burgdörfer, and Peter Hommelhoff. Large optical field enhancement for nanotips with large opening angles. *New Journal of Physics*, 17(6):063010, 2015.

[12] Sergey Bozhevolnyi and Francisco García-Vidal. Focus on plasmonics. *New Journal of Physics*, 10(10):105001, 2008.

[13] P.R. West, S. Ishii, G.V. Naik, et al. Searching for better plasmonic materials. *Laser & Photonics Reviews*, 4(6):795–808, 2010.

[14] F. Fabre, G. Petite, P. Agostini, and M. Clement. Multiphoton above-threshold ionisation of xenon at 0.53 and 1.06 m. *Journal of Physics B: Atomic and Molecular Physics*, 15(9):1353–1369, 1982.

[15] P Kruit, H G Muller, J Kimman, and M J van der Wiel. Relation between 'above-threshold' ionisation probabilities and continuum-continuum matrix elements. *Journal of Physics B: Atomic and Molecular Physics*, 16(13):2359–2368, 1983.

[16] P. Agostini, F. Fabre, G. Mainfray, G. Petite, and N. K. Rahman. Free-Free Transitions Following Six-Photon Ionization of Xenon Atoms. *Physical Review Letters*, 42(17):1127–1130, 1979.

[17] N B Delone and V P Krainov. *Multiphoton Processes in Atoms: Second Edition*, volume 53. Springer Berlin Heidelberg, Berlin, Heidelberg, 2000.

[18] Farhad H. M. Faisal. *Theory of Multiphoton Processes*. Springer US, Boston, MA, 1987.

[19] L.V. Keldysh. Ionization in the Field of a Strong Electromagnetic Wave. *Journal of Experimental and Theoretical Physics*, 20(5):1945–1957, 1965.

[20] F V Bunkin and M V Fedorov. Cold Emission of Electrons from Surface of a Metal in a Strong Radiation Field. *Soviet Physics JETP*, 21(5):896–899, 1965.

[21] M V Ammosov, N B. Delone, and V P Krainov. Tunnel ionization of complex atoms and of atomic ions in an alternating electromagnetic field. *Sov. Phys. JETP*, 64:1191–1194, 1986.

[22] G. G. Paulus, W. Nicklich, Huale Xu, P. Lambropoulos, and H. Walther. Plateau in above threshold ionization spectra, 1994.

[23] Georg Wachter, Christoph Lemell, Joachim Burgdörfer, et al. Electron rescattering at metal nanotips induced by ultrashort laser pulses. *Physical Review B - Condensed Matter and Materials Physics*, 86(3), 2012.

[24] Johannes Schötz. Attosecond experiments on plasmonic nanostructures. *LMU Master Thesis*, 2014.

[25] P. B. Corkum. Plasma perspective on strong field multiphoton ionization. *Physical Review Letters*, 71(13):1994–1997, 1993.

[26] G. Herink, D. R. Solli, M. Gulde, and C. Ropers. Field-driven photoemission from nanostructures quenches the quiver motion. *Nature*, 483(7388):190–193, mar 2012.

[27] M. Lewenstein, Ph Balcou, M. Yu Ivanov, Anne L'Huillier, and P. B. Corkum. Theory of high-harmonic generation by low-frequency laser fields. *Physical Review A*, 49(3):2117–2132, 1994.

[28] M. Busuladžić, A. Gazibegović-Busuladžić, and D. B. Milošević. High-order above-threshold ionization in a laser field: Influence of the ionization potential on the high-energy cutoff. *Laser Physics*, 16(2):289–293, 2006.

[29] Hirofumi Yanagisawa, Sascha Schnepp, Christian Hafner, et al. Temporal and spectral disentanglement of laser-driven electron tunneling emission from a solid. *arXiv:1405.0609v2*, page 4, 2014.

[30] Robert Szipöcs, Kárpát Ferencz, Christian Spielmann, and Ferenc Krausz. Chirped multilayer coatings for broadband dispersion control in femtosecond lasers. *Optics Letters*, 19(3):201–203, 1994.

[31] Sebastian Koke, Christian Grebing, Harald Frei, et al. Direct frequency comb synthesis with arbitrary offset and shot-noise-limited phase noise. *Nature Photonics*, 4(7):462–465, 2010.

[32] Takao Fuji, Jens Rauschenberger, Alexander Apolonski, et al. Monolithic carrier-envelope phase-stabilization scheme. *Optics letters*, 30(3):332–334, 2005.

[33] Pierre Tournois. Acousto-optic programmable dispersive filter for adaptive compensation of group delay time dispersion in laser systems. *Optics Communications*, 140(4-6):245–249, 1997.

[34] C. Le Blanc, P. Curley, and F. Salin. Gain-narrowing and gain-shifting of ultra-short pulses in Ti: sapphire amplifiers. *Optics Communications*, 131(November):391–398, 1996.

[35] W Tomlinson, R Stolen, and C Shank. Compression of optical pulses chirped by self-phase modulation in fibers. *J. Opt. Soc. Am. B*, 1(2):139–149, 1984.

[36] P. Colosimo, G. Doumy, C. I. Blaga, et al. Scaling strong-field interactions towards the classical limit. *Nature Physics*, 4(5):386–389, 2008.

[37] Giulio Cerullo and Sandro De Silvestri. Ultrafast optical parametric amplifiers. *Review of Scientific Instruments*, 74(1):1, 2003.

[38] Hanieh Fattahi. Third-generation femtosecond technology. *LMU PhD Thesis*, 2013.

[39] Ieva Gražulevičiūtė, Milda Skeivytė, Enrika Keblytė, et al. Supercontinuum generation in YAG and sapphire with picosecond laser pulses. *Lithuanian Journal of Physics*, 55(2):110–116, 2015.

[40] M. Kulawik, M. Nowicki, G. Thielsch, et al. A double lamellae dropoff etching procedure for tungsten tips attached to tuning fork atomic force microscopy/scanning tunneling microscopy sensors. *Review of Scientific Instruments*, 74(2):1027, 2003.

[41] Max Eisele, Michael Krüger, Markus Schenk, Alexander Ziegler, and Peter Hommelhoff. Note: Production of sharp gold tips with high surface quality. *Review of Scientific Instruments*, 82(2):026101, 2011.

[42] Doo Jae Park, Bjoern Piglosiewicz, Slawa Schmidt, et al. Strong Field Acceleration and Steering of Ultrafast Electron Pulses from a Sharp Metallic Nanotip. *Physical Review Letters*, 109(24):244803, 2012.

[43] Ryan M. Roth, Nicolae C. Panoiu, Matthew M. Adams, et al. Resonant-plasmon field enhancement from asymmetrically illuminated conical metallic-probe tips. *Optics Express*, 14(7):2921, 2006.

[44] Nicolas Behr and Markus B. Raschke. Optical Antenna Properties of Scanning Probe Tips: Plasmonic Light Scattering, Tip−Sample Coupling, and Near-Field Enhancement. *The Journal of Physical Chemistry C*, 112(10):3766–3773, 2008.

[45] Eric W. Weisstein. Prolate Spheroidal Coordinates. *http://mathworld.wolfram.com/ProlateSpheroidalCoordinates.html*.

[46] Parry Moon and Domina Eberle Spencer. *Field Theory Handbook*. Springer Berlin Heidelberg, Berlin, Heidelberg, 1971.

[47] G G Paulus, W Becker, W Nicklich, and H Walther. Rescattering effects in above-threshold ionization: a classical model. *Journal of Physics B: Atomic, Molecular and Optical Physics*, 27(21):L703–L708, 1994.

[48] M. F. Kling, J. Rauschenberger, A. J. Verhoef, et al. Imaging of carrier-envelope phase effects in above-threshold ionization with intense few-cycle laser fields. *New Journal of Physics*, 10, 2008.

[49] T F Gallagher. Above-Threshold Ionization in Low-Frequency Limit. *Physical Review Letters*, 61(20):2304–2307, 1988.

[50] R. Bormann, M. Gulde, A. Weismann, S. V. Yalunin, and C. Ropers. Tip-Enhanced Strong-Field Photoemission. *Physical Review Letters*, 105(14):147601, 2010.

[51] Hiroyuki Kawano. Effective work functions for ionic and electronic emissions from mono- and polycrystalline surfaces. *Progress in Surface Science*, 83(1-2):1–165, 2008.

[52] Sergey Zherebtsov, Thomas Fennel, Jürgen Plenge, et al. Controlled near-field enhanced electron acceleration from dielectric nanospheres with intense few-cycle laser fields. *Nature Physics*, 7(8):656–662, 2011.

[53] F. Süßmann, L. Seiffert, S. Zherebtsov, et al. Field propagation-induced directionality of carrier-envelope phase-controlled photoemission from nanospheres. *Nature Communications*, 6:7944, 2015.

[54] Martin J. G. Lee. Field emission of hot electrons from tungsten. *Physical Review Letters*, 30(24):1193–1196, 1973.

[55] Michael Krüger, Markus Schenk, and Peter Hommelhoff. Attosecond control of electrons emitted from a nanoscale metal tip. *Nature*, 475(7354):78–81, 2011.

Acknowledgments

First and foremost, I would like to thank Prof. Matthias Kling for giving me the opportunity to work in his group. His valuable inputs during the group meetings, occasional encouragement and his enthusiasm in the project created a very motivating and positive atmosphere to work in. I also thank Prof. Manfred Kappes for agreeing to be the internal supervisor for this thesis.

I especially thank Johannes Schötz for his help in the lab during the initial days, and always making time for me to discuss or answer my doubts, throughout my stay in the group. I thank Hirofumi Yanagisawa for sharing his valuable experience in the field over long hours of discussions. I am grateful to Pawel Wnuk, Harald Fuest and Marcel Neuhaus for providing excellent support with the operation of the newly built 1800 nm laser and appreciate the support from Philipp Rupp and Christian Burger with the operation of the 700 nm laser during the initial days. I thank William Okell for sharing his valuable inputs on the experiment and all the members of the Kling group, who have been very supportive colleagues at, and outside work. I am thankful to Michael Förster and Timo Paschen from the group of Peter Hommelhoff, for providing us with the nanotips along with Christian Späth and Benjamin Duschner from the group of Prof. Ulf Kleineberg, for providing us with SEM images of the same. Apart from specific project, I also thank Mrs. Monika Wild for her administrative support.

In the end, I am very grateful to my friends and especially my family, who have been very supportive all throughout.